Whispering gallery mode microresonators: Fundamentals and applications

G. C. Righini([1]), Y. Dumeige([2]), P. Féron([2]), M. Ferrari([3]), G. Nunzi Conti([1]),
D. Ristic([3]) and S. Soria([1])

([1]) CNR, Istituto di Fisica Applicata "Nello Carrara", MDF Lab
       50019, Sesto Fiorentino, Italy
([2]) UMR Foton, ENSSAT - 22305 Lannion, France
([3]) CNR, Istituto di Fotonica e Nanotecnologie - 38123 Trento, Italy

Summary. — Confinement of light into small volumes has become an essential requirement for photonic devices; examples of this trend are provided by optical fibers, integrated optical circuits, semiconductor lasers, and photonic crystals. Optical dielectric resonators supporting Whispering Gallery Modes (WGMs) represent another class of cavity devices with exceptional properties, like extremely small mode volume, very high power density, and very narrow spectral linewidth. WGMs are now known since more than 100 years, after the papers published by John William Strutt (Lord Rayleigh), but their importance as unique tools to study nonlinear optical phenomena or quantum electrodynamics, and for application to very low-threshold microlasers as well as very sensitive microsensors, has been recognized only in recent years. This paper presents a review of the field of WGM resonators, which exist in several geometrical structures like cylindrical optical fibers, microspheres, microfiber coils, microdisks, microtoroids, photonic crystal cavities, etc. up to the most exotic structures, such as *bottle* and *bubble* microresonators. For the sake of simplicity, the fundaments of WGM propagation and most of the applications will be described only with reference to the most common structure, *i.e.* microspherical resonators.

PACS `42.60.Da` – Resonators, cavities, amplifiers, arrays, and rings.
PACS `42.25.Bs` – Wave propagation, transmission and absorption.
PACS `42.55.Sa` – Microcavity and microdisk lasers.
PACS `42.79.Gn` – Optical waveguides and couplers.

1. – Introduction

Optical resonators play an extremely important role in modern optics, being fundamental not only in any laser device, but also as etalons for optical filtering and as tools for very accurate measurements and for nonlinear optics experiments [1-5]. Bulk optical resonators, however, have a number of limitations due to their size, weight, alignment and stability problems. Most of these problems were overcome by the integrated optics approach, and a particular class which has emerged in the recent years and has found its way into many applications is that of integrated ring resonators [6].

Another rapidly emerging class of miniaturized optical resonators, also exploiting the confinement of light beams, is constituted by dielectric structures having circular symmetry, which sustain the so-called Whispering Gallery Modes, that can be interpreted as electromagnetic waves that circulate and are strongly confined within the structure. In terms of geometric optics, the confinement is described by the optical rays which are totally internally reflected and focused by the surface itself. The definition of whispering gallery modes is due to John William Strutt (Lord Rayleigh), who studied the characteristics of the so-called Whispering Gallery, namely the circular gallery, 32 m in diameter, running around the interior of the dome of St Paul's Cathedral in London, at about 30 m above the floor. It had got this name because a whisper against its wall at any point is audible to a listener with an ear held to the wall at any other point around the gallery. Lord Rayleigh correctly attributed this phenomenon to the refocusing effect of the curved surface as the sound travels along the gallery, and in the years 1910-1912 published *The Problem of the Whispering Gallery* [7,8]; he also suggested that such propagation modes would exist for electromagnetic waves as well, and could find practical applications due to the extreme confinement of the field. The phenomenon is now well known; for instance, the Museum of Science and Industry in Chicago opened in 1938 a Whispering Gallery as a permanent exhibit to demonstrate the wonders of sound wave communication, and nowadays a popular place is the ceramic arches gallery located on the Grand Central Terminal, New York (and one can find several "demonstration" videos on Youtube!).

As the optical resonances in these structures are a function of their morphology (*i.e.* their geometry) and dielectric properties (refractive index), they are sometimes referred to as MDRs (Morphology-Dependent Resonances) [9,10]. Due to minimal reflection losses and to potentially very low material absorption, these resonators can reach exceptionally high-quality factors $Q = \lambda/\Delta\lambda$ (where λ is the wavelength at which a resonance occurs and $\Delta\lambda$ the linewidth of the resonant wavelength), up to 10^{11}, compared to values around 10^5 for the best Fabry-Perot resonators. As an example, a theoretical analysis indicated values of Q close to 10^5 for ideal lossless photonic-bandgap Fabry-Perot resonators, reducing to $Q > 2000$ for real dielectric materials [11]. The extraordinary high-Q values of WGM resonators lead to very high energy density (of the order of GW/cm^2), very narrow resonant-wavelength lines ($< 100\,KHz$ at $1550\,nm$), and a lengthy cavity ringdown: these properties make these structures of great interest for lasers, optical and RF communications, quantum optics and electrodynamics, and sensing [12-14].

Since Lord Rayleigh's papers hundred years ago, WGMs have been deeply studied at sound, optical and microwave wavelengths in various systems, including cylindrical and toroidal geometries, micrometer-sized liquid droplets, and glass and crystal spheres. A pioneering approach to the study of the resonances in a suitably shaped object made of a dielectric material was published by Richtmyer in 1939 [15]; he showed that a spherical microparticle could sustain high-resonance modes. Garrett *et al.*, in 1961, first noticed that spherical resonators for optical waves could be used as laser resonators; they observed pulse laser oscillation in highly polished Sm^{+3}-doped CaF_2 spheres with diameter between one and two millimeters [16].

In recent years WGM resonators (WGMRs) have attracted an increasing attention, and a growing number of papers have been published, investigating structures from the simplest ones, namely cylindrical optical fibers [17] and microspheres [18, 19] to fiber coils [20], microdisks [21-24], microtoroids [25-28], photonic crystal cavities [29-31], microcapillaries [32, 33], etc., up to the most exotic structures, such as bottle [34, 35] and bubble [36-38] microresonators. The goals of circuit integration and cost-saving mass-manufacturing processes have addressed much of the research towards planar structures, like ring- and disk-resonators, which can be microfabricated onto wafer substrates using conventional integrated-circuit deposition and etching techniques. Microspheres, on the contrary, appear to be less easily integrable but, on the other hand, they have the advantage of being the simplest three-dimensional WGM resonator. Microspherical resonators are typically ten to hundred micrometers in diameter, and they are often fabricated in silica glass by simply melting the tip of a conventional single-mode fiber; such a spherical cavity can support very complicated modes with equatorial, radial, as well as polar field dependencies. Liquid microspheres have also been investigated, and indeed early experiments studied WGMs and laser emission in liquid microdroplets flying in air [39-42]. Tzeng *et al.*, for instance, observed laser action from individual ethanol droplets ($60\,\mu m$ diameter) containing Rhodamine 6G dye and pumped by a cw laser at $514.5\,nm$; laser emission was at wavelengths corresponding to the morphology-dependent resonances of a spherical droplet [39]. Micrometer-sized droplets of Rh-6G solution in water and ethanol were also investigated by Biswas *et al.* [42], who irradiated the droplets by high-intensity nanosecond pulses from a frequency-doubled Nd:YAG laser. Coupling of the spontaneous fluorescence emission with natural resonant modes of the spherical droplets resulted in stimulated emission, with each droplet behaving like a laser cavity with a value of Q of the order of 7×10^4. In a recent paper, the fluorescence and lasing characteristics of Rh-6G-doped water microdroplets have been exploited for the identification and sizing of these particles in a spray [43].

Another advantage of microspherical resonators is the easiness of applying a functional coating; covering silica microspheres with polymers, dyes or nanoparticles has proved very effective in enhancing their optical properties or adding new functions [44-55]. All these characteristics motivate our choice to focus the present review on microspherical structures, even if other geometries will be considered as well.

After reviewing the basic concepts of WGM propagation (sect. **2**), we will discuss the problems of efficient coupling of light into/out a microresonator and of measurement of the Q-factor (sect. **3**). A brief review of fabrication processes of microspherical resonators is given in sect. **4**, while sect. **5** is devoted to the specific problems and properties of coated microspheres. Finally, among the possible applications, specific attention will be focused on microspherical biosensors (sect. **6**).

2. – Whispering gallery modes: Basic properties

The electromagnetic surface oscillation in optical cavity is traditionally termed whispering gallery mode. These modes are commonly imagined as closed-trajectory rays confined within the cavity by almost total reflections from the curved surface of the resonator. Whispering gallery modes are not only supported by sphere but also by cylindrical-, spheroidal- and toroidal-shaped open dielectric resonators. These WGM resonators can have an extremely high-quality factor Q that makes them promising devices for applications in optoelectronics and experimental physics. Table I gives some examples of measured Q-factors for different kinds of WGM resonators and different materials (fused silica or crystals).

For the sake of clarity we consider in this section only the case of spherical resonators and their associated properties. A simple geometric picture (fig. 1) leads to the concept of resonances associated with WGMs. We consider (fig. 1(a)) a dielectric sphere (with refractive index N) of radius $a \gg \lambda$ placed in vacuum and a ray of light propagating inside, hitting the surface with angle of incidence i. If $i > i_c = \arcsin(1/N)$, then total internal reflection (TIR) occurs. Because of spherical symmetry, all subsequent angles of incidence are the same, and the ray is trapped. If this ray strikes the surface at near-glancing incidence ($i \approx \pi/2$), the trapped ray propagates close to the surface, and traverses a distance $\approx 2\pi a$ in a round trip. If one round trip exactly equals ℓ wavelengths in the medium (ℓ is an integer), then one expects a constructive interference to occur. In terms of size parameter the resonance condition is $x = 2\pi a/\lambda \approx \ell/N$. The number of wavelengths ℓ in the circumference can be identified as the angular momentum in the usual sense. Indeed, let us consider the ray in fig. 1(a) as a photon. Its momentum is $p = \hbar k = \hbar 2\pi N/\lambda$, where k is the wave number. At near-glancing incidence ($i \approx \pi/2$), the angular momentum, denoted as L (fig. 1(b)), is $L \approx ap = a2\pi\hbar N/\lambda = \hbar\ell$. As an

TABLE I. – *Order of magnitude of measured Q-factors associated with passive Whispering Gallery Resonators differing in shape and materials.*

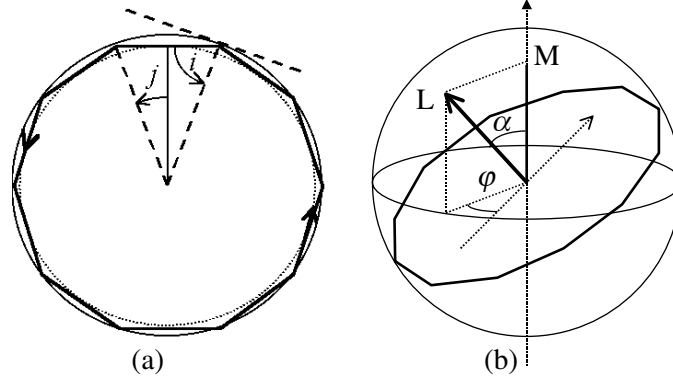| Resonator	Material	Q-factor	Reference
Sphere	silica	10^8–10^9	[56, 57]
Torus	silica	10^8	[25]
Truncated spheroid	CaF_2	10^{11}	[58]
Truncated spheroid	MgF_2	10^8	[59]

Fig. 1. – (a) Ray of light propagation by TIR in a spherical cavity. (b) Angular momentum L associated with WGM and its M projection on the polar axis.

example, if we consider a $50\,\mu$m radius silica sphere at $\lambda \approx 1.5\,\mu$m, we obtain $\ell > 300$ and consequently, in the optical domain, whispering gallery modes can be viewed as high angular momentum electromagnetic modes in which light propagates by repeated total internal reflection at grazing incidence with the proper phase condition after circling along the resonator surface.

Investigation of the optical phenomena occurring in dielectric spheres has a long and vast history. The Lorentz-Mie theory [60-62] gives us a strict analytical solution to the problem of scattering of electromagnetic wave by a homogeneous sphere of arbitrary radius and with arbitrary dielectric constant. This theory can be applied to calculate parameters of scattered radiation. Using this theory, other optical phenomena such as the morphology-dependent resonances [9, 10] in fluorescence spectra can be understood.

In the framework of classical electrodynamics we can use the so-called Hansen's method [63] where solutions of the vectorial Helmholtz equation have angular dependence described by vectorial spherical harmonics [64] defined as

$$
(1) \qquad
\begin{cases}
\vec{X}_\ell^m = \vec{\nabla} Y_\ell^m \times \vec{r}/\sqrt{\ell(\ell+1)}, \\
\vec{Y}_\ell^m = r\vec{\nabla} Y_\ell^m/\sqrt{\ell(\ell+1)}, \\
\vec{Z}_\ell^m = Y_\ell^m \hat{r}.
\end{cases}
$$

In this picture, each WGM field $\{\vec{E}_{\ell m}^P(\vec{r}), \vec{B}_{\ell m}^P(\vec{r})\}$ is numbered by a set P, ℓ, m. The index P describes the polarization of the oscillation, that can be transverse electric (TE) (*namely* $\vec{r} \cdot \vec{E} = 0$) or transverse magnetic (TM) (*namely* $\vec{r} \cdot \vec{B} = 0$). The mode number ℓ indicates the order of the spherical harmonic Y_ℓ^m that describes the angular field distribution. This function is the eigenfunction of the square of the orbital momentum operator (*i.e.*, $L^2 Y_\ell^m = \hbar^2 \ell(\ell+1) Y_\ell^m$). The index m is called the azimuthal mode number (with $L_z Y_\ell^m = \hbar m Y_\ell^m$, *i.e.* the projection on the polar axis). It can take $2\ell + 1$ values

from $-\ell$ to ℓ. Formally we can express the fields for both polarizations as

(2)
$$\begin{cases} \vec{E}_{\ell m}^{\text{TE}}(\vec{r}) = E_0 \frac{f_\ell(r)}{k_0 r} \vec{X}_\ell^m(\theta, \varphi), \\ \vec{B}_{\ell m}^{\text{TE}}(\vec{r}) = \frac{E_0}{ic} \left(\frac{f_\ell'(r)}{k_0^2 r} \vec{Y}_\ell^m(\theta, \varphi) + \sqrt{\ell(\ell+1)} \frac{f_\ell(r)}{k_0^2 r^2} \vec{Z}_\ell^m(\theta, \varphi) \right), \end{cases}$$

(3)
$$\begin{cases} \vec{E}_{\ell m}^{\text{TM}}(\vec{r}) = \frac{E_0}{N^2} \left(\frac{f_\ell'(r)}{k_0^2 r} \vec{Y}_\ell^m(\theta, \varphi) + \sqrt{\ell(\ell+1)} \frac{f_\ell(r)}{k_0^2 r^2} \vec{Z}_\ell^m(\theta, \varphi) \right), \\ \vec{B}_{\ell m}^{\text{TM}}(\vec{r}) = -\frac{iE_0}{c} \frac{f_\ell(r)}{k_0 r} \vec{X}_\ell^m(\theta, \varphi), \end{cases}$$

where a is the radius of the sphere, N the relative index of refraction. $f_\ell(r) = \psi_\ell(Nk_0 r)$ for $r < a$ and $f_\ell(r) = A\psi_\ell(k_0 r) + B\chi_\ell(k_0 r)$ for $r > a$ are solutions of a Riccati-Bessel radial equation. $\psi_\ell(\rho) = \rho\, j_\ell(\rho)$ and $\chi_\ell(\rho) = \rho\, n_\ell(\rho)$, where j_ℓ and n_ℓ are, respectively, spherical Bessel and Neumann functions.

We can note that the radial equation

(4)
$$\frac{\mathrm{d}^2 f_\ell(r)}{\mathrm{d}r^2} + \left[N^2(r)k^2 - \frac{\ell(\ell+1)}{r^2} \right] f_\ell(r) = 0$$

is very similar to the Schrödinger equation of a particle with a mass M in a pocket-like pseudo-potential V_{eff} (depending on energy)

(5)
$$\left[-\frac{\hbar^2}{2M}\Delta + V_{\text{eff}}(r) \right] \psi(r) = E\psi(r),$$

where $E = \frac{\hbar^2 k^2}{2M}$ and

(6)
$$V_{\text{eff}}(r) = \frac{\hbar^2}{2M} \left\{ [1 - N^2(r)]k^2 + \frac{\ell(\ell+1)}{r^2} \right\},$$

This pseudopotential takes into account the refractive-index discontinuity $N - 1$ at the surface of the sphere and its curvature. This effective-potential approach thoroughly analyzed by Nussenzveig [65] provides good physical insight into many properties of the WGMs which appear as quasi-bound states of light. The number of peaks in the radial distribution of the field inside the sphere (fig. 2) leads directly to the definition of a radial number n. The lowest-lying state is confined near the bottom of the potential well, *i.e.* as close as possible to the surface of the sphere, and is expected to occur for $\ell \approx Nka \approx Nx$, the maximum value of the angular momentum. Light trapped into this mode can escape out of the sphere only by tunneling across the potential barrier which extends as far as Na for this state. The very long evanescent tail of this quasi-bound state implies a very weak coupling to the outside $N = 1$ medium and extremely high Q-factors. The quasi-bound state energy domain is limited, thus only few n values correspond to WGMs.

2·1. *Approximated positions of resonances*. – The whispering gallery modes are modes of an open system. In such a system a dissipation of energy occurs because the electro-magnetic fields leak from the optical cavity. Expressions (2) and (3) should satisfy the
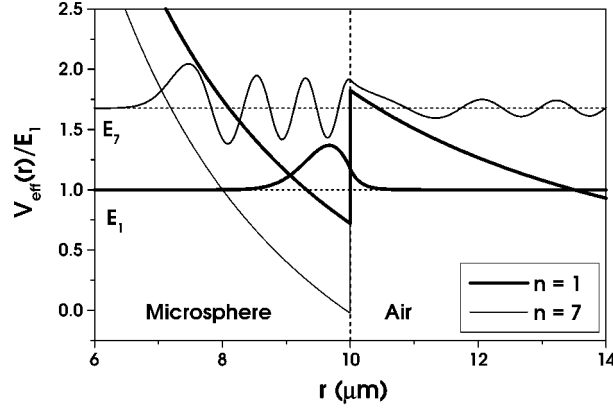
Fig. 2. – Effective potential and associated radial functions for an equivalent particle and turning point for fundamental energy E_1 ($n = 1$) and E_7 ($n = 7$) in the case of a TE mode ($\ell = 100$) in a silica microsphere ($a = 10\,\mu$m, $N = 1.45$).

conditions on the sphere boundary. The condition of continuity of tangential components of the fields allows us to find equations for the positions of resonances.

$$
(7) \qquad
\begin{cases}
\psi_\ell(Nk_0a) = A\psi_\ell(k_0a) + B\chi_\ell(k_0a), \\
P\psi'_\ell(Nk_0a) = A\psi'_\ell(k_0a) + B\chi'_\ell(k_0a),
\end{cases}
$$

where $P = N$ for TE polarization ($P = N^{-1}$ for TM). The exact solutions go through the determination of constants A and B and lead to complex frequencies. As we consider resonators with diameters large relative to λ the radiative leakage of the energy is small. A good approximation consists in assuming the radiative part outside the sphere as negligible; thus, the resonance condition expressed in size parameter $x = 2\pi a/\lambda$ can be written as

$$
(8) \qquad P\frac{\psi'_\ell(Nx)}{\psi_\ell(Nx)} = \frac{\chi'_\ell(x)}{\chi_\ell(x)}
$$

and translating the spherical Bessel and Neumann functions to their cylindrical counterparts we obtain

$$
(9) \qquad P\frac{J'_\nu(Nx)}{J_\nu(Nx)} = \frac{N'_\nu(x)}{N_\nu(x)},
$$

where $\nu = \ell + 1/2$.

The characteristic equation (9) determines in fact the relation between the wave number k and the sphere radius a. Because these equations have many roots, they determine an infinite set of wave vectors (eigenfrequencies) for a given radius of the sphere. In this case, it is necessary to introduce the third index n (radial number), which indicates to what number of the root of eq. (9) one or another value of the wave vector (eigenfrequency) corresponds. Note that this characteristic equation is independent of the index m, so that the modes of a dielectric body of an ideal spherical shape prove

to be degenerated over this index. This degeneration is removed when the shape of a dielectric body deviates from a sphere.

The study of the properties of WGMs involves first of all the calculation of the roots of characteristic equations and, even under this approximated equation, the solutions x have to be numerically evaluated. In order to obtain analytical expressions for the resonances positions and because we deal with modes associated with large index ℓ, it is convenient to use the appropriate approximation of Bessel functions for calculations of these roots. An appropriate approximation should be chosen bearing in mind that the argument of the Bessel function for a WGM near the sphere surface is of the order of its index. In this case, the Bessel and Neumann functions $J_\nu(Nx)$ and $N_\nu(x)$ as well as their derivatives $J'_\nu(Nx)$ and $N'_\nu(x)$ in eq. (9) can be expressed as asymptotic series in powers of $\nu^{-1/3}$ and Airy functions [66]. This method first developed by Lam *et al.* [10] and also presented in a previous paper [18] allows the resonance positions to be obtained

$$(10) \qquad Nx^P_{\ell,n} = \nu + a_{1n}\nu^{1/3} + a_0\nu^0 + a_{-1n}\nu^{-1/3} + \cdots,$$

with $a_{1n} = 2^{-1/3}\alpha_n$, $a_0 = -\frac{P}{\sqrt{N^2-1}}$ and $a_{-1n} = \frac{3}{10}2^{-2/3}\alpha_n^2$ where α_n are roots of the Airy function $Ai(-z)$ and associated with the radial order n. Using a similar development, the WGM resonances were experimentally studied by Schiller and Byer [67], where an excellent agreement of the observed spectra with the prediction of the Mie theory was pointed out.

For larger sphere radii we can use an eikonal approach [56, 68, 69]. Under this semi-classical approach we find naturally a radial index n bounded as

$$(11) \qquad 0 < n - \frac{1}{4} < \frac{1}{\pi}\left(\ell + \frac{1}{2}\right)\left(\sqrt{N^2-1} - \arccos(1/N)\right),$$

with $x_{\text{eff}} < \ell + 1/2 < Nx_{\text{eff}}$ ($x_{\text{eff}} = 2\pi a_{\text{eff}}/\lambda$) where a_{eff} is the sum of the sphere radius a and the additional optical path δ_P associated with the Goos-Hänchen effect depending on the polarization P. In this case we find the same development as in eq. (10) for the approximated positions of resonances where we have to replace the root α_n of the Airy function by its semiclassical approximation

$$(12) \qquad \alpha_n \rightarrow \left[\frac{3\pi}{2}\left(n - \frac{1}{4}\right)\right]^{2/3}.$$

In a recent paper Gorodetsky and Fomin [69] analyzed, as a practical example, a spheroidal dielectric cavity and they showed how this geometrical interpretation allows the expansion of the method on arbitrarily shaped axisymmetric bodies.

As mentioned above, the eigenfrequencies for modes with the same index ν (*i.e.* $\ell + 1/2$) but different indices m are degenerated. This degeneration is removed when the shape of a dielectric body deviates from a sphere. For a spheroid (prolate or oblate) with a small eccentricity $e = (r_p - r_e)/a$, where r_p and r_e are, respectively, the polar (r_p) and equatorial (r_e) radii, we can calculate a correction to the resonance frequency. Considering a prolate spheroid (fig. 3), the perimeter ($p_0 = 2\pi a$) of an ideal sphere is changed into

$$(13) \qquad p = p_0\left(1 + \frac{\Delta p}{p_0}\right) \approx 2\pi a\left[1 + \frac{e}{6}(1 - 3\cos^2\alpha)\right],$$
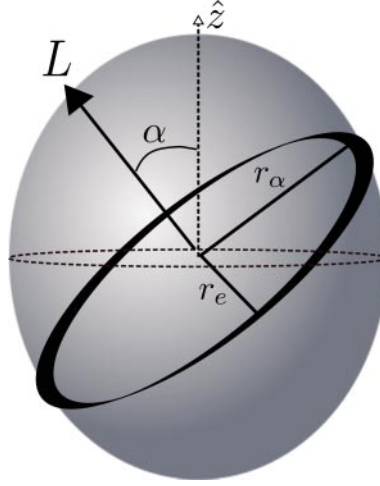
Fig. 3. – Prolate spheroid, $r_e = \bar{r}(\pi/2)$, $r_\alpha = \bar{r}(\pi/2 - \alpha)$ where $\bar{r}(\theta) = a[1 + e(3\cos^2\theta - 1)/3]$ is the parametric radius of the ellipse.

with $\cos\alpha = |m|/(\ell + 1/2)$. Finally, we obtain

$$(14) \qquad N x^P_{\ell,m,n} \approx N x^P_{\ell,n} \times \left[1 + \frac{e}{3}\left(1 - 3\frac{\ell - |m|}{\ell}\right)\right].$$

Expression (14) shows that the deviation of the shape of a dielectric body from a sphere not only removes the degeneration over the index m but also shifts the WGM frequency. This deviation does not remove the degeneracy in sign of m (*i.e.* the counterpropagating waves have the same frequencies). This type of degeneracy is removed by the coupling that appears between the frequency-degenerated waves due to their scattering. Scattering can be caused both by the resonator surface roughness and by the inhomogeneities of the substance density. This type of scattering is commonly called the Rayleigh scattering.

From eq. (14) we deduce the main properties of a WGM spectrum. By analogy with a Fabry-Perot interferometer, we can define a pseudo-Free Spectral Range (pseudo FSR) of the cavity $\Delta\nu^{\Delta\ell}_{n,\ell} = c(x_{n,\ell+1} - x_{n,\ell})/2\pi a$, which corresponds to the spacing between two modes with the same polarization and with the same n but which only differ by one unit of their quantum number ℓ. To a first approximation

$$(15) \qquad \Delta\nu^{\Delta\ell}_{n,\ell} \simeq \frac{c}{2\pi N a}.$$

We can also derive the spacing between two adjacent modes labeled as TE and TM and with fixed values of n and ℓ

$$(16) \qquad \Delta\nu^{\mathrm{TE,TM}}_{n,\ell} \simeq \frac{c}{2\pi N a}\frac{\sqrt{N^2 - 1}}{N}.$$

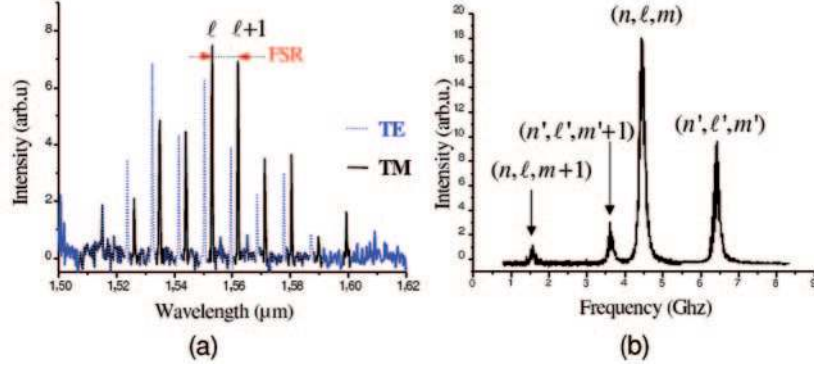For given n and ℓ values, considering a low ellipticity and $|m| \approx \ell$ the relative frequency

Fig. 4. – (a) WGM fluorescence spectrum of Er:ZBLAN microsphere coupled by prism; (b) fine structure of the TM peak at $1.562\,\mu$m.

shift with respect to the spherical shape is

$$(17) \qquad \frac{\Delta\nu_{n,\ell,m}}{\nu_{n,\ell}^0} = -\frac{e}{6}\left(1 - 3\left(\frac{|m|}{\ell + 1/2}\right)^2\right),$$

where $\nu_{n,\ell}^0$ is the resonance frequency of a (n,ℓ) mode at a given polarization P associated with an ideal sphere. All these properties are clearly pointed out with experiments on erbium-doped resonators [70, 71]. Figure 4 presents results obtained with a $56\,\mu$m diameter microsphere doped with 0.2% by weight of erbium. The spectral characteristics of the emission around $1.55\,\mu$m were analyzed with a $0.1\,$nm resolution optical spectrum analyzer. The fluorescence spectrum (fig. 4(a)) presents a discrete feature (the digitalization of the fluorescence spectrum associated with the bulk material), which is characteristic of the collection through WGMs, with mainly two series of peaks associated with TE and TM modes and at this resolution apparently associated to the $n = 1$ radial order. According to eq. (15) the FSR can be approximated by $\Delta\nu = 1137\,$GHz (measured as $1120 \pm 20\,$GHz) and the spacing between TE and TM is $810 \pm 20\,$GHz close to the calculated $\Delta\nu_{n,\ell}^{\mathrm{TE,TM}}$. A close examination of the TM peak at $1.562\,\mu$m was possible using a Fabry-Perot (FSR $= 10\,$GHz, finesse $= 170$) and we obtained (fig. 4(b)) 4 peaks distinguished by (n, ℓ, m) and (n', ℓ', m') values revealing an eccentricity of the order of 0.01%.

2`2. *Quality factor of a whispering gallery mode.* – The imaginary part of the eigenvalue of the wave number associated with a resonance (n, ℓ, P) determines the decay caused by the fact that, unlike a flat surface, the total internal reflection from a curved surface does not exist and leads to a radiation of the wave from the dielectric sphere. Such decay can be called the radiative decay. Corresponding to this phenomenon we define a radiative quality factor

$$(18) \qquad Q_{\mathrm{rad}} = \frac{\mathrm{Re}(k_{0,n,\ell})}{\mathrm{Im}(k_{0,n,\ell})}.$$

Using a semiclassical (Wentzel Kramers Brillouin; WKB) approximation for the Riccati-Bessel radial solutions, one can find [56]

$$(19) \qquad Q_{\text{rad}} \approx x \exp\left[2\nu\, g\left(\frac{x}{\nu}\right)\right],$$

with $g(y) = -\sqrt{1-y^2} + \arg\cosh(1/y)$, x the size parameter and $\nu = \ell + 1/2$. Taking into account low radial orders, we can assume $x/\ell \approx 1/N$ and the function g can be replaced by its tangent, which leads to

$$(20) \qquad Q_{\text{rad}} \approx \frac{\ell}{N} \exp\left[2\ell\, g\left(\frac{1}{N}\right)\right] \times \exp\left[-2\sqrt{N^2-1}\,\frac{Nx-\ell}{N}\right].$$

Using eq. (10) we can develop an expression depending on the radial order n and polarization P. This approximation shows that Q_{rad} decreases as n increases and that for a given mode the radiative Q-factor associated with the TM polarization is slightly lower than the value associated with the TE polarization. Table II presents results obtained with eq. (20) assuming $Nx_{n,\ell} \approx \ell + 1/2$, $\ell = 117$ (sphere diameter $D = 40\,\mu\text{m}$) and $\ell = 294$ (sphere diameter $D = 100\,\mu\text{m}$). For higher ℓ values the radiative Q-factor increases astronomically. This means that, although the internal reflection is not total, it is close to the total reflection for sufficiently large values of ℓ, and the intrinsic Q-factor (noted Q_0 in the following) of the WGM is determined by other mechanisms that cause losses in WGMs. In this connection, it is convenient to introduce the partial Q-factors Q_j related to each type of losses and to describe Q_0 by the well-known expression $Q_0^{-1} = \sum_j Q_j^{-1}$.

TABLE II. – *Examples of Q_{rad} at $\lambda = 1.55\,\mu$m for a $N = 1.5$ microsphere. $D = 2a$ is the diameter of the sphere.*

$Q_{\text{rad}} = 4.24 \times 10^{23}$	$D = 40\,\mu\text{m}$
$Q_{\text{rad}} = 2.51 \times 10^{57}$	$D = 100\,\mu\text{m}$

The main limit of the WGM Q-factor is related to the contribution Q_{mat} associated with absorption and bulk Rayleigh scattering in the material constituting the microresonator. Considering an attenuation β in dB/km, Q_{mat} can be approximated by

$$(21) \qquad Q_{\text{mat}} \approx \frac{4.3 \times 10^3}{\beta}\frac{2\pi N}{\lambda}.$$

For the undoped silica glass used for optical fibers ($\beta \sim 0.2\,\text{dB/km}$ at $\lambda = 1.55\,\mu\text{m}$) it turns out that $Q_{\text{mat}} \approx 10^{11}$. The experimental Q-factor of silica microspheres is much lower (between 10^8 and 10^9) [57,72,73] and we have to take into account a contribution Q_{cont} which denotes the losses introduced by surface contaminants during the fabrication process. Gorodetsky *et al.* [57] explained this effect by absorption of radiation by a nanolayer of molecules (first of all by water molecules) adsorbed on the microsphere surface. This fact was later confirmed experimentally [73].

As last contribution to Q_0 we have to introduce $Q_{\text{s.s}}$ which denotes scattering losses due to residual surface inhomogeneities. In the literature we can find many expressions

for $Q_{\text{s.s}}$. In 1989, Braginsky *et al.* [74] gave a model derived from planar optics [75]. This expression takes into account only the root-mean-square (r.m.s.) size σ of the inhomogeneities.

$$(22) \qquad Q_{\text{s.s}} \approx \frac{3\lambda^2 \ell^{10/3}}{16\pi^5 \sigma^2 N^2 n^{5/2}}\,.$$

Introducing the correlation length of the inhomogeneities B and the diameter of the sphere D, Gorodetsky *et al.* [57] gave in 1996 the following expression:

$$(23) \qquad Q_{\text{s.s}} = \frac{\lambda^2 D}{2\pi^2 \sigma^2 B}\,.$$

This model was refined in 1998 by Vernooy *et al.* [73], who wrote a new expression

$$(24) \qquad Q_{\text{s.s}} \approx \frac{3N^2(N^2+2)^2 \lambda^{7/2} D^{1/2}}{(4\pi)^3 (N^2-1)^{5/2} \sigma^2 B^2}\,.$$

In 2000, Gorodetsky *et al.* [76] obtained the factor $Q_{\text{s.s}}$ for a TE mode in the following form:

$$(25) \qquad Q_{\text{s.s}} = \frac{K_{\text{TE}}}{K_{\text{TE}}+1} \frac{3\lambda^3 a}{8\,N\,\pi^2 B^2 \sigma^2}\,,$$

where K_{TE} is the ratio of the complete scattered power over the power scattered into the angles satisfying definite angular cutoff conditions. These expressions of $Q_{\text{s.s}}$ were given without derivation or only partial derivation except those of Vernooy *et al.* [73] grounded in a review [77]. At fixed values of σ and B, the $Q_{\text{s.s}}$ factor increases with the resonator radius. Nevertheless, any residual roughness on the surface of the resonator
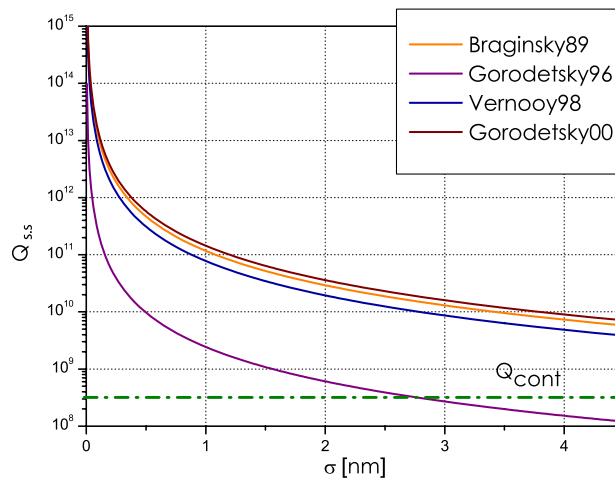

Fig. 5. – Comparison of the evolution of $Q_{\text{s.s}}$ *versus* σ, with $B = 5\,\text{nm}$ and $D = 100\,\mu\text{m}$, as given by eq. (22) noted Braginsky89, eq. (23) noted Gorodetsky96, eq. (24) noted Vernooy98 and eq. (25) noted Gorodetsky00 (see [68].)

results in serious limitation on the achievable WGM Q-factor. With amorphous host material, the resonator formed by surface tension forces during the fusion has nearly a defect-free surface characterized by molecular-scale inhomogeneities. For instance a fused silica resonator easily presents scattering parameters $\sigma \leq 3\,\text{nm}$ and $B \simeq 5\,\text{nm}$ [73] but in this case the diffusion of atmospheric water into the material fixes the upper limit for the intrinsic Q-factor Q_0 to Q_{cont} (fig. 5). This figure presents a comparison of these models considering $100\,\mu\text{m}$ diameter sphere in a $N = 1.45$ dielectric material (silica). The calculations correspond to the best confined $(n = 1, \ell, \ell)$ TE-polarized WG mode with $\ell = 293$. For millimeter-sized resonator, Savchenkov *et al.* [58, 14] have fabricated with polishing techniques crystalline optical resonators with very high Q-factor ($Q > 10^{11}$), limited in value only by the absorption of the material (Q_{mat}), and exceeding that of surface-tension-formed resonators.

3. – Microresonator light coupling

3˙1. *Coupling and dispersion regime*. – WGM microcavities are intrinsically high quality resonators and the key point for applications is the efficiency of light coupling from the outside. Figure 6 shows a schematic view of a spherical WGM resonator and its associated access line which represents any coupling system as will be discussed later.

Due to the high finesse of the resonator, we can consider each resonance ω_0 individually (the angular frequency ω_0 corresponds to a $\nu^P_{n,\ell,m}$ defined using eq. (17)). The input signal field s_{in} is coupled to the resonator mode (whose amplitude is noted as u) with a characteristic lifetime τ_e. The light trapped inside the resonator can escape from the cavity i) through radiative or absorptive processes with a characteristic duration τ_0 and ii) through back coupling to the output field s_{out} in the access line, still with a characteristic duration τ_e.

The intrinsic photon lifetime τ_0 is related to the intrinsic Q-factor by $Q_0 = \omega_0 \tau_0/2$ and we can now define the external Q-factor Q_e by $Q_e = \omega_0 \tau_e/2$. The overall Q-factor Q is deduced from the intrinsic and external Q-factors values by

$$(26) \qquad \frac{1}{Q} = \frac{1}{Q_0} + \frac{1}{Q_e}$$

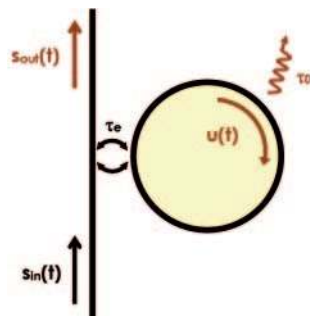the photon lifetime τ in the cavity is then defined by $Q = \omega_0 \tau/2$. Using the coupled mode

Fig. 6. – Sketch of a WGM resonator coupled to its access line.

theory (CMT) [78] the dynamic evolution of the system can be calculated by integrating

$$(27) \qquad \frac{\mathrm{d}u}{\mathrm{d}t} = \left(j\omega_0 - \frac{1}{\tau} \right) u(t) + \sqrt{\frac{2}{\tau_e}} s_{\mathrm{in}}(t),$$

and the output field can be deduced from the mode amplitude by

$$(28) \qquad s_{\mathrm{out}}(t) = -s_{\mathrm{in}}(t) + \sqrt{\frac{2}{\tau_e}} u(t).$$

In the stationary regime at the angular frequency ω, the input field can be written $s_{\mathrm{in}}(t) = s_0 e^{j\omega t}$; the mode amplitude is thus given by

$$(29) \qquad u(t) = \frac{\sqrt{\frac{2}{\tau_e}} s_0 e^{j\omega t}}{j(\omega - \omega_0) + \frac{1}{\tau}}.$$

Using eq. (28) and eq. (29), we can define the linear transfer function $x(\omega)$ of the compound system by

$$(30) \qquad x(\omega) = \frac{s_{\mathrm{out}}(t)}{s_{\mathrm{in}}(t)} = \sqrt{T} e^{j\phi},$$

where T is the intensity transfer function and ϕ is the phase shift introduced by the system. Introducing the frequency detuning $2\pi\delta = \omega - \omega_0$, we can express the amplitude transfer function $x(\omega)$ as

$$(31) \qquad x(\delta) = \frac{1/\tau_e - 1/\tau_0 + 2\pi j\delta}{1/\tau_e + 1/\tau_0 + 2\pi j\delta}.$$

The intensity transmission spectrum $T = |x|^2$ thus reads

$$(32) \qquad T(\delta) = \frac{(1/\tau_e - 1/\tau_0)^2 + 4\pi^2\delta^2}{(1/\tau_e + 1/\tau_0)^2 + 4\pi^2\delta^2}.$$

In fig. 7, we report the value of the intensity transmission at resonance $T(\delta = 0)$ for different values of optical losses. The relative values of τ_0 and τ_e determine the resonator coupling regime [59]

- $\tau_0 < \tau_e$, the losses predominate and the resonator is undercoupled.

- $\tau_0 = \tau_e$, the losses are equal to the coupling rate, the transfer function drops to zero: the resonator is critically coupled. For a given optical loss value, the amount of transfered power from the access line to the resonator is maximal.

- $\tau_0 > \tau_e$, the resonator is overcoupled.

- $1/\tau_0 \to 0$, the resonator is lossless and the coupled system is fully transparent: $T(\delta) = 1$.

- $0 > \tau_0 > -\tau_e$, there is gain inside the resonator and the system acts as an amplifier operating in a narrow frequency band.
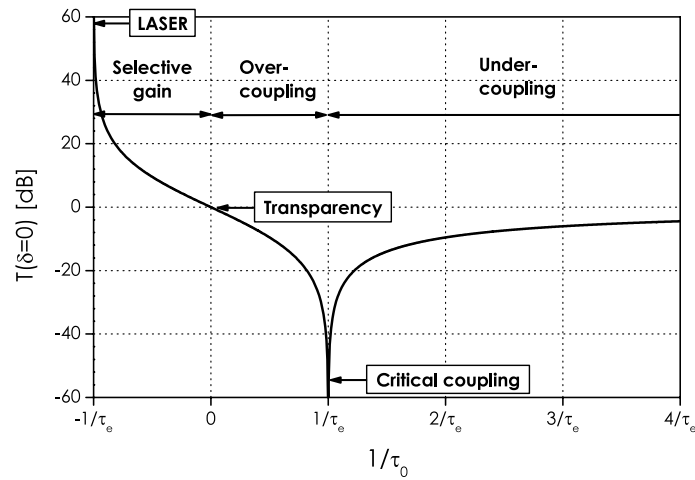
Fig. 7. – Linear intensity transmission at resonance $T(\delta = 0)$ as a function of resonator intrinsic lifetime τ_0 corresponding to intrinsic losses.

In the passive regime, the sole measurement of the transmission function $T(\delta)$ cannot give coupling regime since τ_0 and τ_e play the same role in eq. (32). If one wants to fully determine the coupling regime, the dispersive properties associated to the phase shift part of the transfer function must also be measured. Figure 8 shows the group delay defined as $\tau_g = \mathrm{d}\phi/\mathrm{d}\omega$ as a function of optical losses in the resonator. With our definition, $\tau_g(\delta = 0) < 0$ corresponds to a positive delay referring to the slow light regime whereas $\tau_g(\delta = 0) > 0$ corresponds to a negative delay referring to the fast light regime [79]. For passive resonators (defined by $\tau_0 \geq 0$), the dispersion regime unambiguously gives the coupling regime. The fast light regime corresponds to the undercoupling regime and the slow light regime refers to the overcoupled regime [59].
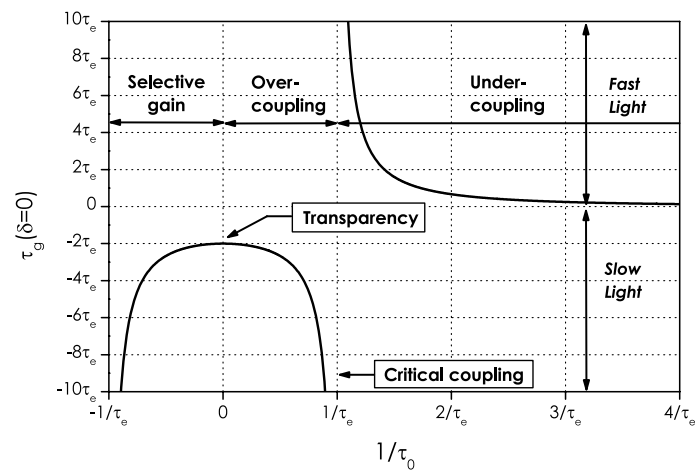

Fig. 8. – Group delay at resonance $\tau_g(\delta = 0)$ as a function of resonator intrinsic lifetime.
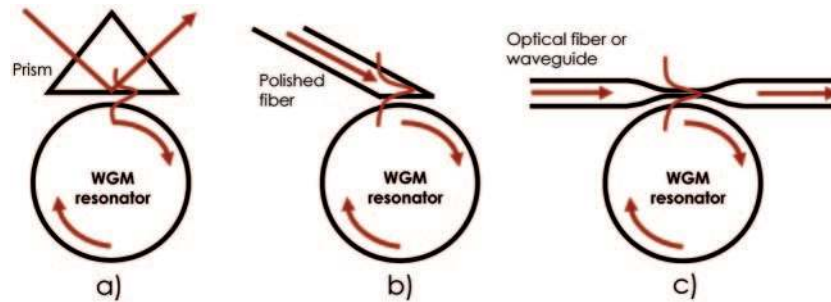
Fig. 9. – a) Prism coupling using frustrated total internal reflection. b) Slant-cut optical fiber coupling. c) Tapered fiber or optical waveguide coupling.

As a conclusion, from an experimental point of view, stationary transmission measurements can reveal the coupling regime only for a critically coupled resonator [80]. In the other cases, the coupling regime can be discriminated by phase shift measurements using interferometric methods [81] or pulse propagation delay measurements in the time domain [82].

3'2. *Overview of coupling method*. – WGM optical coupling using propagative free beams is not efficient because of the really weak radiative transfer to WGMs which can be seen as quasi-bound state of light trapped inside a dielectric material. Several methods have been developed to overcome this drawback. They all rely on energy exchange between a WGM and the evanescent part of guided modes or total internal reflection waves. The prism coupling configuration described in fig. 9(a), based on frustrated total internal reflection, is the oldest method used to couple light in WGM microresonators [74, 83, 84]. This approach can be compacted using an angle polished optical fiber instead of a prism [85] as schematized in fig. 9(b). More recently, tapered fibers (see fig. 9(c) with micrometer or smaller diameter have been used to critically couple high-Q-factor WGM resonators [80, 86]. Using this latter technique, it is possible to obtain the total transfer of the incoming power to the microresonator mode [80]. In the domain of integrated optics, optical waveguides are used to efficiently couple light inside WGM disks or microspheres [87-89]. In the latter case the coupling efficiency can be adjusted by controlling the gap between the optical waveguide and the resonator.

3'3. *Experimental methods to measure coupling parameters*. – In this section we present a simple and accurate high-Q-factor measurement method well adapted to WGM resonators, based on the analysis of the intensity transmission transient profile.

3'3.1. Stationary approach. The most common method used to measure the Q-factor for high- and ultra-high-quality microresonators consists in linearly scanning the frequency of a narrow probe laser at the input of the resonator and to simultaneously record its transmission $T(t)$ (fig. 10). The amplitude $|s_{\mathrm{in}}(t)|$ is kept constant whereas the central frequency of the laser ν is linearly swept. The source is thus modeled by a monochromatic signal whose instantaneous frequency is written as $\nu(t) = \nu_i + \tilde{V}_S t$, where $\tilde{V}_S$ is the frequency sweeping rate. The laser probe is attenuated only when it is tuned to the resonator frequency ν_0. Experimentally, we observe, in the time domain, a dip in the transmission of the resonator. An accurate calibration of $\tilde{V}_S$ allows the frequency
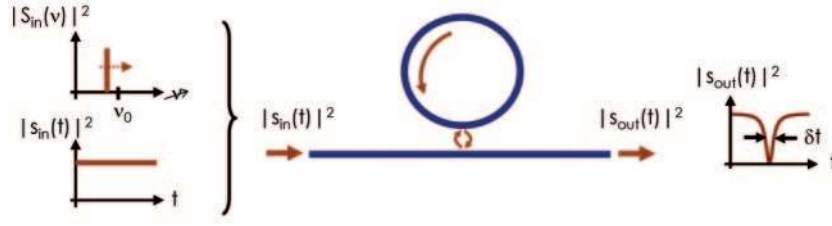
Fig. 10. – Schematic view of the Q-factor measurement method.

spectrum to be measured. In particular the measurement of the width δt in the time domain gives the bandwidth of the resonator by $\delta_{1/2} = \delta t \times \tilde{V}_S$.

3˙3.2. Dynamical approach. The previous method is valid only for very low sweeping rates $\tilde{V}_S \ll \tilde{V}_0 = 2/(\pi\tau^2)$ in order to record the stationary response of the resonator. $\tilde{V}_0$ is the scanning rate corresponding to a frequency band $1/(\pi\tau)$ which is the bandwidth of the resonator swept during $\tau/2$. For higher-frequency sweeping rates, the excitation cannot be considered as stationary anymore and a ringing phenomenon strongly modifies the profile of the transmission [58,90,91]. This effect comes from the beating of the input and the intracavity fields. In this case the mode amplitude reads

$$(33) \qquad u(t) = \sqrt{\frac{2}{\tau_e}} s_0 \exp\left(j\omega_0 t - \frac{t}{\tau} \right) \cdot \left[f(t) - f(0) + \frac{1}{j(\omega_i - \omega_0) + \frac{1}{\tau}} \right],$$

with $\omega_i = 2\pi\nu_i$ and where $f(t)$ can be expressed using the complex error function $\mathrm{erf}(z)$ with $z \in \boldsymbol{C}$ and $V_S = 2\pi\tilde{V}_S$

$$(34) \qquad f(t) = -\sqrt{\frac{j\pi}{2V_S}} \exp\left[\frac{-j(2\pi\delta_i - j/\tau)^2}{2V_S} \right] \cdot \mathrm{erf}\left(\frac{j/\tau - 2\pi\delta_i - V_S t}{\sqrt{2jV_S}} \right).$$

The ringing effect can be used to obtain the phase of the field inside the resonator and thus to determine the coupling regime. Figure 11(a) shows the transmission of a given Q resonator in the over- and undercoupling regimes in the stationary or very-slow-frequency sweeping regime. Since τ_0 and τ_e play the same role in the transmission function T the
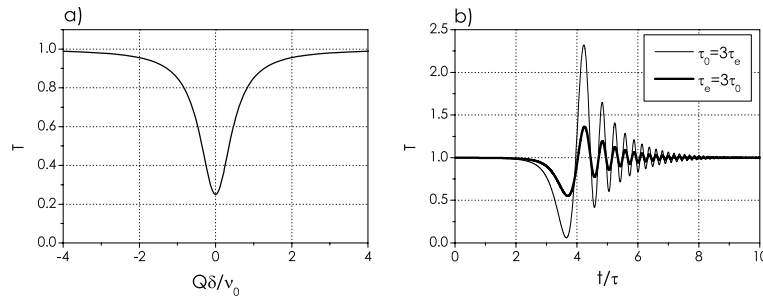

Fig. 11. – a) Stationary transmission profile for a resonator in the undercoupling ($\tau_e = 3\tau_0$) and overcoupling ($\tau_0 = 3\tau_e$) regimes: the two curves are perfectly superimposed. b) Transmission in the two regimes in the dynamic case, when the frequency sweeping rate is $\tilde{V}_S = 2.25\tilde{V}_0$.

two responses are exactly the same. By increasing the frequency sweeping rate, the responses of each coupling regime are strongly different, which allows the coupling or dispersion regime to be known as shown in fig. 11(b).

3˙3.3. *Experiments.* The experimental method consists in numerically comparing the transient response of the resonator to the analytical model (eqs. (33) and (34)) and then deducing the experimental parameters: $\tilde{V}_S$, τ_0 and τ_e. Note that in this method $\tilde{V}_S$ does not need to be calibrated and its value is given by the numerical procedure. We performed two sets of measurement to characterize i) a lithium niobate (LN) disk and ii) a silica microsphere. The physical characteristics of the two devices are given in table III. Light is coupled in the resonator using a LN waveguide in the case of the LN disk and a tapered single-mode fiber in the case of the silica microsphere.

TABLE III. – *Physical description of the LN disk and the silica microsphere experimentally tested. The characterization results are presented as well.*

	LN disk	Silica microsphere
Diameter	4.7 mm	145 μm
Thickness	1 mm	-
Coupling method	LN waveguide (width 6 μm)	Tapered fiber (diameter $< 3\,\mu$m)
τ_0	193 ns	360 ns
τ_e	6930 ns	1290 ns
$\tilde{V}_S$	10.4 MHz/μs	4.75 MHz/μs
Coupling regime	Undercoupling ($\tau_0 < \tau_e$)	Undercoupling ($\tau_0 < \tau_e$)
Q	1.12×10^8	1.71×10^8

Figure 12 represents the experimental set-up used to measure high-Q-factors. The probe is a tunable narrow external cavity laser diode. The device under test (DUT) is the LN disk or the silica microsphere. We used different optical detectors whose bandwidths
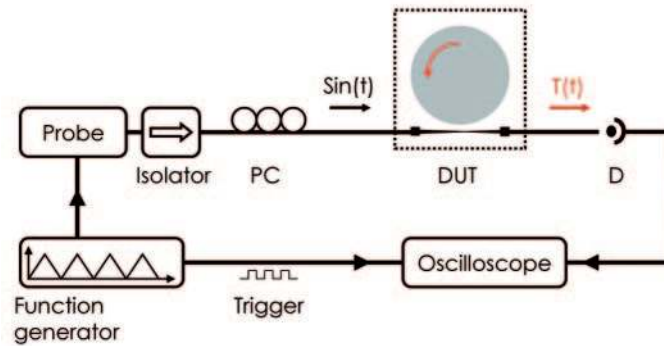

Fig. 12. – Q-factor measurement experimental set-up. The probe laser is a tunable narrow linewidth (150–300 kHz) laser. PC is a polarization controller, D is a photodetector. The DUT (device under test) is either a LN microdisk coupled using a LN waveguide or a silica microsphere coupled using a tapered fiber.
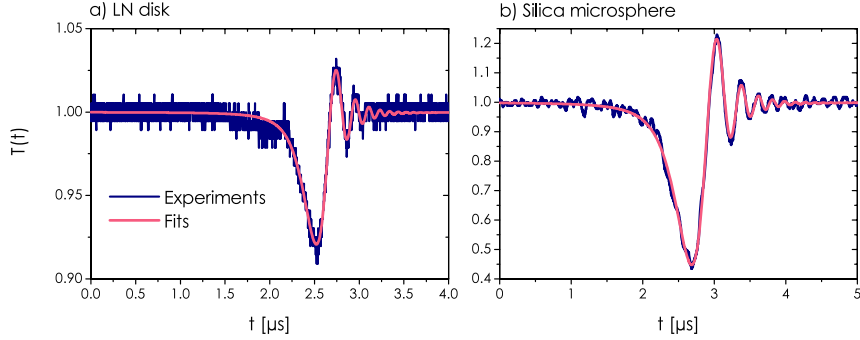
Fig. 13. – Experimental transient profile of the transmission $T(t)$: a) for the LN disk, and b) for the silica microsphere. We have also drawn the numerical fit from which the values of τ_0, τ_e and $\tilde{V}_S$ are inferred.

are larger than 10 MHz. The experimental profiles obtained for the two devices are shown in fig. 13. We also give the numerical fit from which we have deduced the values of τ_0, τ_e and $\tilde{V}_S$: these values are given in table III. In the two cases, taking into account the sweeping rates, the resonator must be undercoupled in order to reach the highest value of the overall Q-factor which corresponds to the intrinsic Q-factor (Q_0).

As a conclusion, the proposed method allows the Q-factor and the coupling regime of a passive WGM resonator to be measured. The method can be extended to amplifying resonators [59]. For high-finesse resonators with modal coupling coming from enhanced Rayleigh backscattering [72,92], the method can be modified to also measure the coupling rate between co- and contra-propagative modes [93].

4. – Fabrication of WGM microresonators

As anticipated in the previous sections, there is a variety of geometries of WGMRs, each of them having its pros and cons; three major parameters must be considered in order to assess the impact of a given type: the achievable value of the Q-factor, the easiness of fabrication, and the integrability. In this section we will briefly review the fabrication techniques of the most common resonating structures.

As concerns the materials, glasses, and in particular pure silica, are the most widely used, even if crystalline materials would guarantee higher performances and additional advantages to these resonators as compared to their amorphous counterparts. As an example, ultimate Q-factors of silica microspheres (10^8–10^9 at about $1.55\,\mu$m) rapidly decrease in usual environment due to diffusion of atmospheric water into the material, while a number of crystals do not absorb moisture. High-purity crystals theoretically have a perfect lattice without inclusions or inhomogeneities and typically have very low intrinsic absorption within their transparency window; Q-factors exceeding 10^{11} and finesse $F > 10^7$ have been achieved in calcium fluoride crystalline disks by the JPL group [94]. The same group also analyzed the fundamental limits of Q-factor of crystalline dielectric resonators, and showed that spontaneous Raman scattering is the main limitation of the quality factor at low temperatures, while stimulated Raman scattering is important at any temperature [95]. Crystals, moreover, often exhibit enhanced nonlinear

or electro-optical properties, which may play an additional role for the implementation of high-performance devices. Crystalline materials, on the other hand, are not suitable for the fabrication of microspherical resonators, which usually requires melting of the material. Melting, in fact, would destroy the crystalline structure and the stoichiometry of the material, also adversely affecting the initial purity. Glasses remain, therefore, the best material for WGM microspheres.

4$^{.}$1. *Cylindrical WGM microresonators*. – Cylindrical WGMRs may be very easy to fabricate, but have the disadvantage that, due to the longitudinal degree of freedom in such a structure, a coupled beam here, as opposed to the WGM in a microcavity, spreads along the cylinder length and eventually vanishes, even if there is no material loss. One of the earliest experiments, intended to show in the most visual manner possible that spiral whispering mode propagation exists within closed optical bodies of circular cross section, was done using machined cylinders from commercial grade polymethyl methacrylate [96]. The simplest cylindrical WGMR, however, is constituted by a small piece of a conventional telecom single-mode optical fiber (chosen due to its high material quality), stripped from coating and suitably cleaned [17,97]. In this case, too, an experimental analysis has shown that if the fiber is tilted (*i.e.* not exactly perpendicular to the in-coupled beam) "spiral" WGMs, tracing a helical path along the fiber, are triggered [98].

Strong WGM resonances can also be obtained with jacket-removed cladding-thinned bent optical fibers [99]. In such a structure, a ray radiates along the tangent from the radiation caustic where the core mode loses its confinement and then is subject to total internal reflection at the boundary between the cladding and the air. Thus, the ray propagates along the fiber wall, forming a WGM. The reason for reducing the cladding thickness is due to a compromise between the need of keeping the mechanical flexibility necessary for tight bending of the fiber without breaking and the capability of controlling the optical path length of the WGM, which depends on the cladding thickness. As to the preparation process itself, first the polymer jacket of a portion of the fiber is removed using a stripping tool and then the cladding is thinned by chemical etching with hydrofluoric acid.

More generally, a very recent paper presents a quantum interpretation of whispering gallery modes in a cylindrical optical microcavity in analogy with quantum mechanical theory [100]. Miniature optical fiber and microfiber coils also exhibit propagation of whispering gallery modes; their fabrication, however, is challenging [101]. The set-up sketched in fig. 14 enables simultaneous drawing, tapering, and coiling of a silica optical fiber. It consists of: i) a rotary gear motor, which performs the rotation of the central rod and coiling of the fiber around it; ii) translation stages for initial positioning of the fiber with respect to the rod; iii) a CO_2 laser to soften the fiber at the initial area of its contact with the rod.

4$^{.}$2. *Toroidal and microdisk WGM resonators*. – Some of the early solid-state lasers [102,103] have to be considered among the first devices effectively exploiting WGM light confinement. Röss, in Germany, fabricated two lasers in cylindrical toroids of ruby (or, more precisely, in rings with polished cylindrical surfaces parallel to the toroid axis), the material being a 0.035% Cr^{+3} ruby of medium quality, with c-axis oriented at 90° to toroid axis. The size of these compact lasers was 13 mm outer diameter, 9 mm or 11 mm inner diameter, 5 mm height [102]. He underlined the outstanding property of this approach which made it possible to combine an extremely high resonator Q with a moderate mode selection leading to quasi-continuous oscillations in an inhomogeneous material like
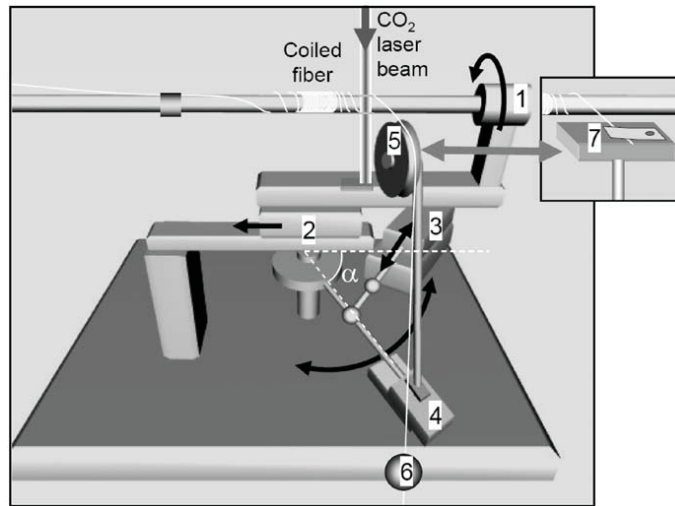
Fig. 14. – Sketch of the experimental set-up for fiber coil fabrication: 1 a rotary gear motor; 2, 3, 4 translation stages; 5 a wheel supporting the incoming fiber; 6 a weight; 7 a fiber clamp. (Reproduced with permission from [101].)

ruby. In the same year (1963) Walsh *et al.*, in U.S.A., also reported pulsed laser operation at room temperature in a ruby ring, exploiting total internal reflection [103]. One of their ring lasers had external diameter $15/16''$ ($23.8\,\mathrm{mm}$), internal diameter $7/8''$ ($22.2\,\mathrm{mm}$), and height $1/8''$ ($3.18\,\mathrm{mm}$); the other one $5/8''$, $9/16''$, and $1/8''$, respectively. The *c*-axis was perpendicular to the plane of both rings, and Cr_2O_3 concentration was 0.05% by weight. The rings were fabricated and mechanically polished by a commercial manufacturer; all surfaces except the inside diameter surface were optically polished. The authors estimated that the Q-value of these cavities was between 10^8 and 10^9, and noted that these values were about two orders of magnitude larger than those measured in silvered rods. Much more recently, efficient Raman lasing has been demonstrated in CaF_2 WGM disk resonators [104, 105]. A low continuous-wave emission threshold of $3\,\mu\mathrm{W}$ was observed in a $5\,\mathrm{mm}$ cavity, made possible by its ultrahigh optical quality factor, of the order of $Q = 5 \times 10^{10}$.

All these millimeter-sized resonators were produced by mechanical polishing, possibly followed by thermal annealing, but the actual procedure could be different. The JPL group, for instance, has developed a fabrication technique which relies on diamond turning (which exploits computer control of a precision lathe) of the crystalline workpiece, followed by a conventional polishing technique [104]. By using the diamond turning process they were also able to realize a special single-mode cavity, formed by a small $5\,\mu\mathrm{m} \times 3\,\mu\mathrm{m}$ waveguide on top of a cylinder. Such a waveguide supported only one WGM per cavity FSR, and Stokes lasing modes were experimentally observed [105]. Alternatively, a more conventional and simpler polishing technique could be used, starting from a small cylinder cut from a CaF_2 blank. The cylinder may be glued onto a cap installed onto a high-speed motor, while a thin thread with a diamond abrasive is used to create a region that supports the whispering gallery modes. Polishing has obviously to be performed in several steps with decreasing diamond grit size; after each step an

accurate cleaning is necessary. The authors underlined that such a technique can be automated, and can allow one to produce disks with a curvature radius down to $10\,\mu$m and below [105].

A similar procedure was used, and reported in a very recent paper [106], to produce high-Q lithium niobate disks of $4.7\,$mm in diameter, made from commercial $3'' \times 1\,$mm thick Z-cut lithium niobate wafers by core drilling a cylinder and thereafter polishing the edge into a spheroidal shape. The polishing procedure of crystalline disks was in this case optimized by using a home-made lapping station, which is shown in fig. 15. The almost spherical profile was obtained through a rotational stage whose pivot point could be finely adjusted. Six successive polishing steps were performed, starting with abrasive disks with grit of 12 and 9 microns, respectively, followed by a finer polishing phase, based on polycrystalline diamond suspensions with decreasing grit sizes (3, 1, 0.25, and 0.05 microns, respectively). After each step a rather critical cleaning procedure using organic solvents was implemented. In this way, it was possible to achieve an intrinsic disk Q-factor of 1.3×10^8, as measured from resonance linewidth and confirmed by ringdown measurements (see table III and fig. 13) [106].

Even if mm-sized disks are more easily integrable than microspheres, still they remain discrete objects, possibly to be coupled to optical integrated circuits; moreover, optical polishing cannot be easily adapted to sub-mm devices. For the development of micron-sized robust integrated devices a much more effective approach is the one first proposed by Vahala's group, demonstrating a process for producing silica toroid-shaped
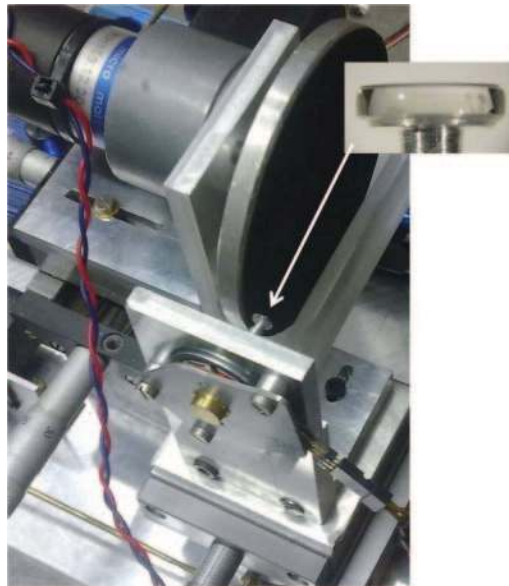

Fig. 15. – Photo of the lapping station for mm-sized disks; a lithium niobate disk, glued to a metal rod, is visible (magnified image in the inset). It is polished by the abrasive (black) cloth pasted onto the rotating plate. The disk axis can be finely tilted, and the contact pressure between the disk edge and the abrasive cloth may be carefully controlled [106].
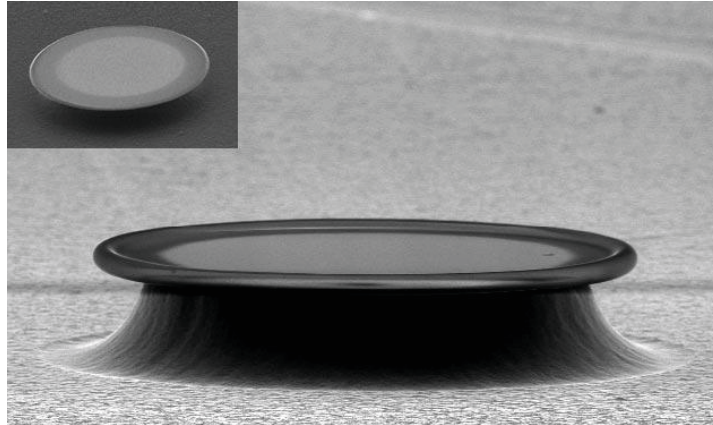
Fig. 16. – Scanning electron micrograph of a silica microdisk after selective reflow treatment with a CO_2 laser. The inset shows the microdisk prior to laser treatment. (Reprinted with permission from [25].)

microresonators-on-a-chip with Q factors in excess of 10^8 [25]. Figure 16 shows a scanning electron micrograph of a silica microdisk, fabricated upon silicon wafers prepared with a $2\,\mu$m layer of silicon dioxide (SiO_2). The fabrication process was composed of four steps: photolithography (creating disk-shaped photo-resist pads typically $160\,\mu$m in diameter); pattern transfer into the silicon dioxide layer; selective dry etch of the exposed silicon; and selective reflow of the patterned silica. By using this process, the group shortly thereafter demonstrated a chip-based (monolithic) microcavity Raman laser, exhibiting ultralow threshold, high efficiency, and single-mode emission. For a microtoroid with diameter $\sim 61\,\mu$m and thickness $\sim 3.7\,\mu$m they measured a quality factor 10^8 and a threshold power (at 1550 nm) $\sim 74\,\mu$W for Raman lasing near 1680 nm [107].

Stimulated emission could be achieved by incorporating erbium (or another rare earth) ions into the toroidal microcavity; this goal has been pursued by a group in Grenoble, that developed a process for the integration of silicon-rich oxide (SRO) layers doped with Er into toroidal microcavities [108]. The SRO:Er thin film was obtained by co-evaporation under NH_3 atmosphere of silicon monoxide and erbium in a high vacuum vessel. Each sample was annealed under forming gas (95% N_2 - 5% H_2) to activate emitters. First, silica microdisks on circular silicon pillars were fabricated by defining the discs by optical lithography in photoresist and transferring them to the silica or SRO layer by wet chemical etching using buffered HF; the silicon substrate was then selectively etched by SF_6/Ar reactive ion etching, forming arrays of silica microdisks on silicon pillars. In a second step, selective reflow treatment with a CO_2 laser was used to form the toroidal microcavities, by taking advantage of the much larger (100:1) thermal conductivity of silicon than silica. Thus, during reflow treatment, only the silica layer is heated, the silicon pillar acting as a heat-sink and cooling the centre of the silica microdisk. This results in a selective melting and smoothing of the edge of the silica disk, without affecting its centre. The final surface roughness of a toroidal microcavity produced in this way is close to that of a liquid droplet, as can be seen in the micrograph of fig. 17.
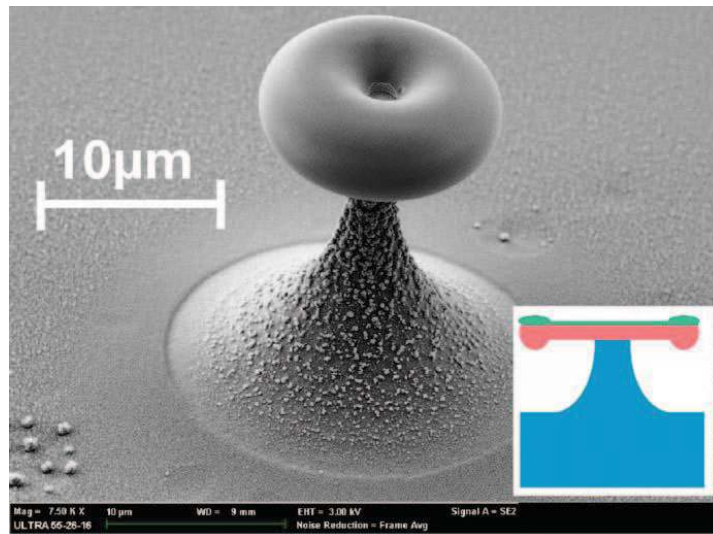
Fig. 17. – Scanning electron micrograph of a toroidal microresonator of diameter $13 \, \mu$m after selective reflow. An SRO:Er layer $200 \, $nm thick had previously been deposited on top of a $2.7 \, \mu$m silica layer. (Reprinted with permission from [108].)

4˙3. *Microspherical WGM resonators*. – One of the great advantages of microspheres is that they may be very easily produced in the laboratory from a large variety of materials, organic and inorganic. As already said, liquid microspheres or microdroplets have been the subject of investigation since the very beginning of this field. Nowadays, polymer microspheres and their dispersions (namely polymer colloids or latex) are widely used, more than in photonics, in medical and biochemical applications, including absorbents, latex diagnostics, affinity bio-separators and drug and enzyme carriers [109]. Polymer colloid chemists are now able to prepare truly monodisperse microspheres, *i.e.* having a monodispersity (ratio of weight-average diameter to number-average diameter) less than 1.005. Polymer microspheres can be prepared either by physical methods, such as emulsification, coacervation and spray-drying, or by chemical methods such as heterogeneous polymerization. Kawaguchi [110] published a review of these methods and of the properties and applications of polymeric microspheres: even if not fully up to date, it remains of large interest. Two recent papers concerning the application of polymer microspheres as WGM resonators also provide indications for their fabrication [111,112]. One of the possible routes consisted in fabricating first a PMMA fiber and then a microsphere by melting the tip of the fiber, just as in the case of silica microspheres; the polymer powder (with a particle size of a few micrometers) was placed in a container inserted in a hot oil bath at a temperature just above the PMMA melting point ($\sim 150\,^{\circ}$C), then PMMA fibers were stretched to a diameter of $125 \, \mu$m or smaller. The Q-factor of the microspheres prepared this way was found to be not so high ($\sim 5 \times 10^4$), most probably due to impurities in the material and surface irregularities caused by uneven heating [111]. The same authors, however, improved the Q-factor up to 10^6 by using another approach: first, impurities in the polymer were removed by dissolving it in chloroform and adding it to a solution of methyl alcohol where the polymer precipitated. Then, the material was passed through a paper filter and again dissolved in chloroform; finally, using a microsyringe, a controlled

drop of the so purified PMMA was placed at the tip of a PMMA fiber. Hollow PMMA spheres could also be obtained by injecting a controlled amount of air into the liquid polymer before depositing it onto the fiber tip.

Polydimethylsiloxane (PDMS) microspheres were also fabricated with a slight modification of the process described above [112]. In order to be able to prepare spheres of diameter smaller than a few hundreds microns, the tip of a tapered fiber was used; thus, the end of a fiber with diameter in the range of 2–$10\,\mu$m was inserted into, and quickly withdrawn from, a prepared PDMS liquid (RTV 184, Dow Corning 5:1). Due to surface tension, a spherical-shaped PDMS cavity supported by the tapered fiber stem was formed with extremely smooth surface. By utilizing fiber tapers with different diameters and adjusting viscosity of the precured PDMS, microspheres with diameters ranging from $100\,\mu$m to 1 mm could be fabricated.

A completely different approach has been reported by Li *et al.*, involving the fabrication of dye molecule-doped microspheres in a microfluidic channel, which can also create arrays onto a chip [113]. A schematic diagram explaining the basics of this process is shown in fig. 18; the upper stream part is a channel junction for spontaneous formation of dye containing droplets based on the well-known hydrodynamic focusing technique. Mineral oil (oil phase) is used for the focusing flow whereas a UV-curable resin (NOA81, Norland) mixed with $10^{-2}\,$mol/L R6G and 5% (volume ratio) of ethanol is used as "aqueous" phase. The down stream is a collection chamber in which the polymer droplets coming from the left side through the connection channel are solidified by UV exposure. Once fabricated, the microspheres, which are highly monodispersed (monodispersivity $\pm 2.1\%$) and size controllable, in a range between 20 and $80\,\mu$m, can be collected and placed in another PDMS chamber, having in- and out-channels. In an
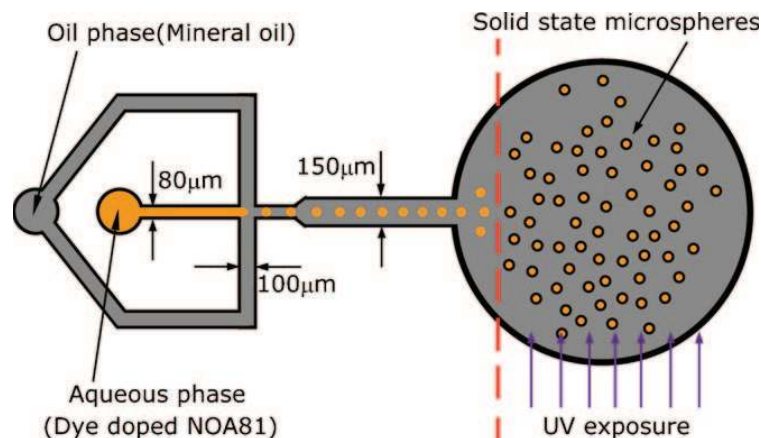

Fig. 18. – Sketch of the microfluidic device for microsphere fabrication. The upper stream part is a cross-channel junction allowing spontaneous formation of dye containing droplets which are photo-curable and monodispersed in size. The down stream part is a collection chamber, in which UV exposure solidifies the droplets coming from the left side connection channel. (Reproduced with permission from [113].)
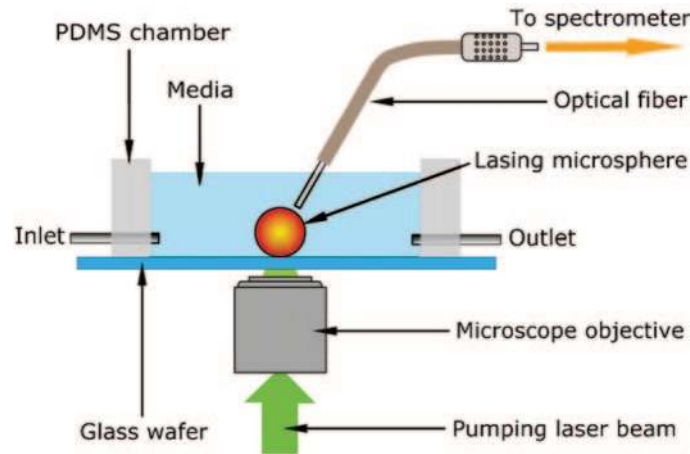
Fig. 19. – Experimental set-up for microsphere excitation and laser output observation. The open chamber is obtained by bonding a PDMS frame (10 mm × 20 mm in size and 3 mm in height) to a glass wafer. The pulse width of the pumping laser was less than 10 ns and the frequency was 20 Hz. (Reproduced with permission from [113].)

experimental test, single microsphere were randomly selected and excited with a pulsed frequency-doubled Nd:YAG laser. The experimental set-up for microsphere excitation and characterization is shown in fig. 19. Laser excitation was achieved by focusing the pump beam though a microscope objective, and fluorescence signal was collected by a multimode optical fiber and transferred to a fiber spectrometer. The optical quality of these R6G-doped WGMRs was poor (a $Q \sim 10^3$ was experimentally inferred, probably limited by the resolution power of the spectrometer used) but high enough to observe lasing in a microsphere of radius 73.87 μm at a threshold of about 16 μJ/mm^2.

The largest number of WGM microspherical resonators, however, is made in glassy materials; pure silica is the first choice, because of the available material purity, but there are several examples of microspheres fabricated in multi-component glasses and in particular in functional glasses. Two main techniques for the fabrication of glass microspherical resonators can be taken into consideration, one based on melting processes, the other one on sol-gel chemistry, and will be briefly described in the following.

4'3.1. Melting of glass microspheres. General-purpose processes, which can be used to fabricate microspheres from a large range of glass compositions, imply either directly producing a glass by melting or using the powder obtained by crushing an available glass. In the former case, several paths can be followed: a very simple one, which has also been used to fabricate Er^{3+}-doped tellurite glass microlasers, consists of melting the oxide components in a furnace and dropping the viscous glass onto a spinning plate [114]. Another process, adopted for a multi-component fluoride glass based on ZrF$_4$, started from melting the raw materials in a vitreous carbon crucible at 1000 °C, inside an induction furnace; then, the molten batch was poured in a fine stream into liquid nitrogen, and the spherical particles which passed through a 50 mesh sieve were collected from the quenched glasses [115]. A problem occurring in such a case was the easy contamination of the sphere surface, in particular by oxidized products, such as Zr-OH and Zr-O; a chemical polishing was therefore required, and it was performed by using an ultrasoni-

cally agitated bath of $ZrOCl_2 - 8H_2O$ dissolved in water. All the operations, except the chemical polishing, were carried out in a dry-nitrogen gas atmosphere.

A different approach, with higher degree of complexity, was involving the use of magnetic levitation to keep the glass sample suspended while heated: containerless melting of glass and fabrication of microspheres from a cubic glass sample (*e.g.* with a size of 4 or 6 mm) in a furnace constructed of a CO_2 laser and a solenoid-type magnet were demonstrated [116, 117]. The glass cube, placed in a platinum cage at the edge of the inner magnet, is made to levitate and there it is melted by the effect of the focused laser beam: a complete glass sphere was thus obtained after cooling. Subsequent polishing to optical grade seems, however, to be necessary [117].

The other general fabrication process implies crushing the selected glass material: as an example, high-Q microspheres were produced by dropping the glass powder through a microwave plasma torch [118]. The re-melted glass grains acquire spherical shape by surface tension before being hardened by the air flow and falling into a proper container. By adjusting the microwave power and the gas flow, it is possible to reach the desired temperature (around 2000 °C for silica-based glasses, 800-900 °C for fluoride glasses), and to produce spheres with a low eccentricity.

Another technique used to produce glass microspheres for general applications made use of a rotating electric arc: microspheres with diameters between 2 and 24 μm were fabricated with a good yield; in fact, by processing of the glass powder, 85% of particles were transformed into microspheres [119]. A number of patents are also covering the subject of glass microsphere fabrication, especially in view of medical applications. With the exception of the magnetic levitation method, which on the other hand requires the previous preparation of a cube with the desired size, a disadvantage of these techniques is that one obtains a number of free spheres with a rather large size distribution and difficult to manipulate. It is therefore necessary to place the produced spheres under an optical microscope and to sort them by size, while also checking their surface quality. The selected spheres may be picked up with a glass capillary connected to a vacuum pump, and then, one at a time, stuck on a tapered fiber.

A very simple and effective method to produce single spheres with the desired diameter is based on the melting of the tip of a glass fiber (see, for instance [18]). It presents the disadvantage of requiring a glass in form of rod or fiber and of permitting the fabrication of only one microsphere at a time, but it is very cheap and allows one a very good control of the microsphere diameter. Upon heating the distal tip of a fiber, *e.g.* a standard telecommunications silica fiber, the glass reflows to form a spherical volume under the influence of surface tension. Due to the high viscosity of silica, the reflowed structure becomes highly spherical (eccentricities of the order of 1–2%), and extremely uniform. The spherical surface has very low intrinsic roughness (measured r.m.s. roughness of the order of 1 nm or lower), and thus presents very small surface scattering losses. Figure 20b) shows a typical silica microsphere, obtained in this way and therefore attached to the fiber stem from which it was formed. The presence of the stem does not affect the resonator's operation because the excited optical modes typically lie in the equatorial plane and thus have negligible overlap with this perturbation region; on the contrary, it is useful for an easy handling of the microsphere.

The reflow process may be induced using different heating sources: an oxygen/butane (or similar) torch [120], a high-power (*e.g.* a CO_2) laser [122, 112], or an electric arc as in a commercial fiber splicer [121]. Fiber splicing is a mechanic-thermal process in which the cleaved fiber ends are heated to a temperature at which they soften. A cleaved tip of the fiber is inserted in one arm of the splicer and a series of arcs are then produced; the
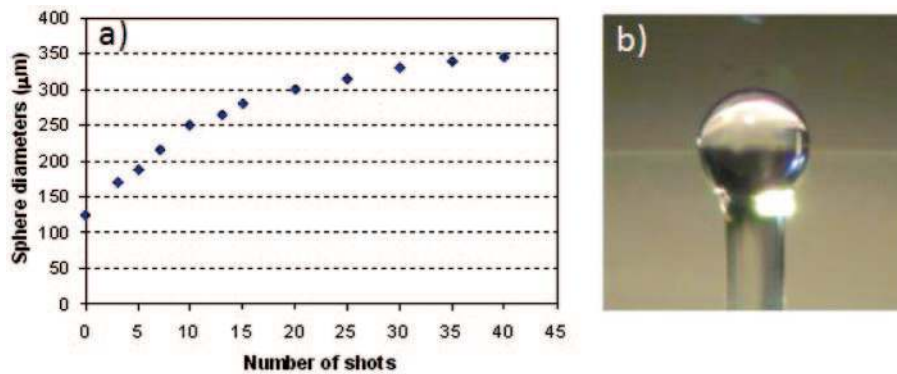
Fig. 20. – a) Size of the microspheres produced at the tip of a standard $125\,\mu$m telecom fiber, as a function of the arc shots in a fiber fusion splicer. b) Optical image of a microsphere with a diameter of about $250\,\mu$m. In the background (out of focus) one can see the coupling tapered fiber [121].

tip partially melts and surface tension forces produce the spherical shape. By accurately controlling the operating parameters of the splicer, reproducible spherical shapes are easily obtained; the size of the spheres increases with the number of arc shots, till it tends to saturate at a diameter of about $350\,\mu$m in the case of standard $125\,\mu$m single-mode fibers [121]. Figure 20a) shows the growth of the sphere diameter with the number of shots; the photo of a typical microsphere, $250\,\mu$m in diameter, is shown in fig. 20b). All these techniques allow one to produce microspheres with diameters usually in the range d to $2d$, where d is the outer diameter of the uncoated fiber; smaller spheres, say from 20 to $100\,\mu$m in the case of conventional telecom fibers, may be obtained by first tapering the fiber in order to reduce the diameter of the tip. The minimum diameter we obtained by using the fiber splicer on tapered fibers was about $40\,\mu$m [121].

$\mathbf{4}$˙3.2. Sol-gel processes for microsphere fabrication. Sol-gel chemistry is attracting a growing interest as a very flexible and cheap method for producing optical materials. The possibility of starting from molecular precursors and elementary building blocks permits to tailor structures at the molecular level and to create new materials with enhanced performances. Two major approaches can be followed when using sol-gel processes to produce spherical microresonators. In fact, besides synthesizing a "bulk" glass with a spherical shape, one can deposit a uniform sol-gel film onto a microsphere previously produced by heating process; the following section is specifically devoted to the coating of microspherical resonators.

Many protocols can be used to realize sol-gel silica spheres: monodisperse silica nanoparticles, in particular, can easily be synthesized via the base-catalyzed hydrolysis of tetraethylorthosilicate (TEOS) [123]; the silica spheres may have a diameter in the range from 150 nm to $2\,\mu$m, with typical size dispersion around 3%. This method cannot be used if one wants to incorporate rare earths into the glass, because lanthanide salts form insoluble lanthanide hydroxides in basic environments. The problem, however, may be overcome by using acid catalysts [124,125]: in this case one obtains silica microspheres with different diameters, ranging from hundred nanometers to approximately 150 micron, always with a very high surface quality.

The synthesis of high-purity dense silica microspheres from organic and inorganic acid hydrolysis of TEOS has been demonstrated using a variety of acid and water mixtures

in the pH range 1.35 to 2.25 with the only restriction of the molar ratio of water/TEOS which varies in the ranges 1.0–1.5 for strong acids and 1.5–4.0 for weak acids [126].

One can also combine the synthesis of a specific glass via sol-gel process with the fabrication of microspheres by melting process; as an example, WGM microlasers were produced by fabricating microspheres with diameters from 40 to $200\,\mu$m by electrical arc, starting from sol-gel silica-alumina glasses doped with high concentration of erbium ions Er^{3+} (from 1250 to 15000 ppm) [127]. In general, sol-gel produced spheres present the advantage of material's very high purity; moreover, composition of bulk and film microresonators may be easily tailored according to the application.

$4\!\cdot\!4.$ *Microbottle and microbubble WGM resonators*. – Considering that WGMs can survive smooth deformation of spheroids, and that two stems, instead of one as with the conventional fiber-based microsphere, make the tuning of a WGM microresonator easier by stretching it [128], Sumetsky *et al.* suggested to use highly oblate resonators, that they called WGM *bottles* (WGB) because of the similarity of their shape to that of the magnetic bottles used in plasma fusion [34]. The properties of highly prolate- or oblate-shaped dielectric microresonators were also theoretically studied by other authors in the following years [129, 69]. The free spectral range (FSR) of such resonators was predicted to be about one order of magnitude smaller than that of microsphere resonators of equal diameter. Bottle microresonators can be fabricated from standard optical fibers in a two-step heat-and-pull process by sequentially microtapering the fiber in two adjacent places to form the bottle [130]; by accurate positioning and stretching the fiber, WGBs of diameter in the range 30 to $40\,\mu$m exhibited Q factors up to 3.6×10^8.

Another effective, and simpler, fabrication technique was developed by following a soften-and-compress approach and using a fiber splicer [131]. The fiber was softened while simultaneously compressed; the use of multiple electric arcs of duration $\sim 1\,$s allowed to controllably soften the glass and to produce robust, double-neck bottle fiber microresonators. Typical geometrical parameters were stem diameter d_s of $125\,\mu$m, neck-to-neck distance L_b of the order of $400\,\mu$m and bottle diameter d_b around $185\,\mu$m; the bottle shape was defined by the softening temperature profile and the applied compression.

An important step towards the integration of devices, especially for sensing applications, was made with the suggestion to use capillaries instead of bulky optical fibers: liquid-core optical ring-resonators (LCORRs) use the evanescent field (in the core) of the WGMs, which are excited into the exterior surface, to detect the refractive-index changes near the interior surface [32]. In this way the liquid or gas under test flows inside the microcapillary and does not perturb the coupling condition of the WGMs with the external tapered fiber; cylindrical resonators, however, as already cited, have the disadvantage of the very critical coupling alignment condition, with the risk of exciting spiral modes (delocalization of WGMs). A further advance was therefore made when *bubble* WGMRs were demonstrated [36, 37]; in fact a microbubble resonator (MBR) (fig. 21) combines the microfluidics advantage of a microcapillary with the characteristics of a microbottle (namely, the presence of real localized WGMs, and the two-stem structure), without introducing significant insertion losses. A fully tunability was demonstrated for a silica MBR, which exhibited a tuning range more than two times larger than the azimuthal FSR of the resonator [36]. As to the fabrication of such structures, the blowing of a silica microbubble is based on the same principle as traditional glass blowing: a gas pressure is applied while the capillary is heated; the control of gas pressure and the uniformity of heating, however, are quite critical, and the fabrication of MBRs with the desired characteristics is challenging [37].
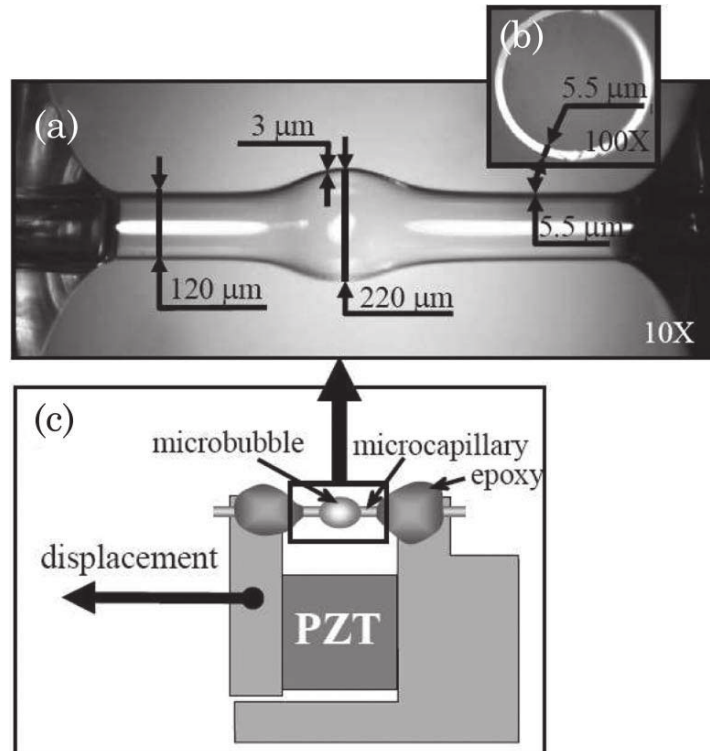
Fig. 21. – A microbottle resonator (MBR). (a): Optical micrograph of the device. (b) (inset): Optical micrograph of the cross-section of the capillary from which the MBR was created. (c): Sketch of the set-up used for the tuning of the resonances by stretching. (Reprinted with permission from [36].)

5. – Microspheres coating by passive or active films

Coating of spherical microresonators is a very promising technique for optimizing their optical properties. Uniformity of the coating is a necessary requirement in order to preserve the high-Q factor of the microresonator, so most of the work done in this field has concerned methods which lead to uniform coatings (fig. 22), although some inhomogeneous coating techniques have been employed too, to produce either half-coated microsphere arrays (spheres which have the coating only on one side of the sphere) [50] or terrace-shaped microresonators (fig. 23) [47].

There are basically two categories of coatings that can be deposited on a microsphere, having lower or higher refractive index than the microsphere itself. A lower-index cladding makes the microsphere insensitive to the surrounding environmental conditions and ensures the stability of the whispering gallery modes. The WGMs stay confined inside the microresonator and can interact with the cladding only through the evanescent wave. As an example, low-index ($N = 1.49$) sol-gel NaO_2-CaO-SiO_2 thin films were deposited onto high-refractive-index ($N = 1.93$) BaO-SiO_2-TiO_2 glass microspheres for the development of Raman lasers [47]. A problem with this kind of system is finding an efficient way of coupling light into the WGMR: in fact, since the evanescent field of the WGMs extends in the cladding but not in the surrounding medium (usually air),
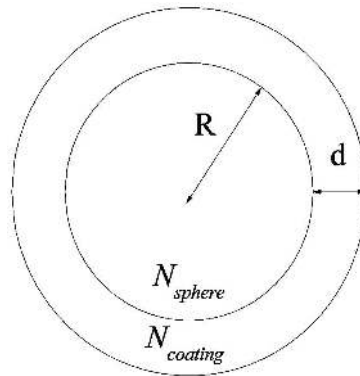
Fig. 22. – A sketch of a uniformly coated microsphere where N_{sphere} is the refractive index of the sphere, N_{coating} is the refractive index of the coating, R is the sphere diameter and d is the thickness of the coating.

evanescent coupling is impossible for such a structure, and direct excitation is required. Then, the reflections at the air-cladding and the cladding-core interfaces become a limiting factor for the efficient coupling of light to the WGMs; a possible solution may be offered by the use of a terrace-microsphere to waveguide coupling scheme, as already demonstrated (fig. 23) [47].

Although the isolation of the microsphere from the environment is an important issue to be addressed for ensuring the applicability of the microresonators in practical devices, from a more fundamental point of view the coating of microresonators with materials having a refractive index higher than the core is much more interesting. Opposite to the previous case ($N_{\text{coating}} < N_{\text{sphere}}$), where the electric field inside the cladding is an evanescent field, here the electric field of the WGMs in the coating is a propagating field, which means that, for a transparent coating, the penetration depth in general is the entire thickness of the coating. The WGMs of such a core-shell structure can have
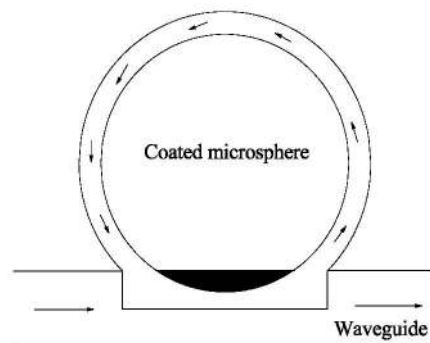

Fig. 23. – A sketch of the terrace-shaped microsphere coupled with a waveguide, adapted from [47]. The arrows indicate the direction of light propagation in the waveguide and in the microsphere and the shaded part indicates the coupling area between the waveguide and the microsphere.

superior characteristics than simple uncoated microspheres, in particular as concerns the thermal stability of the WGM modes. Moreover, the coating can add novel optical functions; the only limitation may be due to the fact that the Q-factor of a microsphere coated with an optically active material is generally reduced compared with the Q-factor of the uncoated one, due to the absorption in the coating and to the scattering on the sphere-coating interface.

The whispering gallery modes of a core-shell structure may be well described by the Aden-Kerker generalization of the Lorentz-Mie scattering theory [132]. Like for the uncoated spheres, the WGMs have spherical symmetry and are characterized by the labels ℓ, m and n. The only difference is that now, to determine the radial part of the WGM fields, three different regions have to be taken into account: the microsphere core —where the fields are propagating waves (represented by the spherical Bessel function only, since the spherical Neumann function would have a singularity in the center of the sphere); the coating —where the fields are also propagating waves, but represented by a linear combination of the spherical Bessel and Neumann functions; and the surrounding medium (usually air) —where the fields are exponentially decaying functions. To solve the eigenfrequency equations, the boundary conditions for the tangential components of the field at the air-coating and sphere-coating interfaces have to be matched. In general, the positions of the WGMs are a function of the refractive indices of the core, shell and surrounding medium, of the radius of the core and of the thickness of the coating. Recently, the exact calculation and comparison of the WGM resonances with the experimental spectra of dye-coated silica microspheres were made and the Aden-Kerker theory was found to accurately reproduce the WGM resonances for small sphere diameters (less than $\sim 14\,\mu$m) [51]. Looking at spheres having diameter in the range 15 to $33\,\mu$m, coated by RhodamineB (RB) with concentration 10^{-4} M (in methanol solution), it was found that an inhibition of the radiative decay time of RB did exist for smaller diameter microspheres. In the presence of the WGMR the electric field of the photon radiated by an oscillating electrical dipole interacts with the microsphere, causing the change of linewidth of the dipole and hence also of the radiative lifetime. The change of the decay times with the size, however, was not observed in spheres coated with a higher $(10^{-3}$ M) RB concentration [51].

Besides Rhodamine-doped coatings [51, 48], spherical microresonators have also been coated by nanocrystalline silicon [50], silica-hafnia glasses and glass-ceramics [133, 134, 18, 135, 136], and HgTe quantum dots [46]. The nanocrystalline silicon is a very promising material for application in optoelectronic devices because of its size-dependent luminescence [137]. A thin (20–100 nm) film of nano-crystalline silicon (nc-Si) was deposited on the top of a fused silica microsphere by using an electron-beam evaporation system, while the bottom of the microsphere was left uncoated [50]. The coated microspheres exhibited WGMs when excited using a 442 nm laser line, but the intensity of the resonances was found to depend strongly on the coupling point because of the inhomogeneity of the coating. To make full advantage of the optical properties of silicon nanocrystals in combination with the spherical microresonators, a deposition method which can guarantee nc-Si coating's uniformity has yet to be developed. A good candidate could be the LPCVD (Low Pressure Chemical Vapor Deposition) method; its advantage over other CVD methods is that here the reactant gases reach the substrate by diffusion rather then by direct flow, and this should make it possible to deposit uniform homogenous films on arbitrary shaped surfaces. The LPCVD method was found to produce films of very low surface roughness, an important requirement for the films to be usable onto WGMRs [138]. Recently, thin LPCVD silicon-rich oxide films (SiO_x, $0 < x < 2$), which
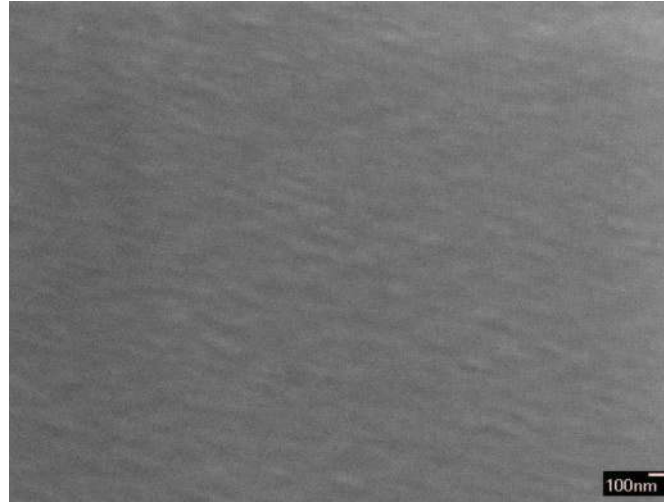
Fig. 24. – SEM image of the surface of a 160 nm thick silicon-rich oxide (SiO_x, $x \approx 0.3$) thin-film–deposited on a silica substrate using the LPCVD method [138].

lead to nc-Si films by thermal annealing, were successfully produced with a very smooth surface (r.m.s. vertical surface roughness less then 3 nm, with lateral surface structures below 50 nm) [138]. Figure 24 shows the SEM image of a silicon-rich oxide thin film [138].

HgTe quantum dots were deposited as a thin layer on the surface of a silica microsphere to act as the active element of a low-threshold laser [46]. Colloidally prepared spherical HgTe nanoparticles were used for the microlaser's active medium coating because of their intense and broad room temperature luminescence spectrum covering the 1200–2000 nm wavelength range. The silica microspheres were coated using a layer-by-layer dip procedure [18, 133]. In particular, polyelectrolyte macromolecules, that adjust their coverage on the silica surface to form transparent shells around the HgTe nanoparticles, were employed to reduce photoinduced corrosion and improve their adherence to the microsphere. Two HgTe-coated microlasers were reported, one having a diameter of 650 μm, pump Q of 2×10^6 (pump wavelength 830 nm), and lasing Q of about 10^7, at around 1620 nm. A threshold pump power of $P_{\text{th}} = 9.41 \pm 2.35 \, \mu$W was estimated. The other microsphere had a diameter of 950 nm, pump Q of 2×10^7, and lasing Q of about 10^8 around 1670 nm, with a threshold absorbed pump power estimated to be less than 200 nW. This work highlights the role of nanostructured coating for the development of very-low-threshold microlasers; their emission wavelength could also be changed by varying stoichiometry and size of the quantum dots.

5'1. *Sol-gel coatings*. – Sol-gel–based coatings are effectively exploited in microspherical resonators due to the fact that the sol-gel process allows for precise control of rare earth ion concentration and high solubility, as well as easy control of the refractive index of the coating. As an example let us mention two papers [139, 127]. Gain functionalization of silica WGMRs was demonstrated by Yang and Vahala [139]. A laser output power of 6 μW was obtained in continuous wave operation for a doped shell of silica activated by an Er^{3+} ion concentration of about $10^{19} \, cm^{-3}$. Hoi *et al.* reported the long-band

lasing in microspheres based on sol-gel silica-alumina glasses doped with a concentration of Er^{3+} ion ranging from 1250 to 15000 ppm [127]. The Q-value of the microsphere was estimated to be more than 10^8 and a maximum laser ouput power of about $10\,\mu W$ was obtained at the wavelength of 1561 nm with a pump power of 40 mW at 976 nm.

Silica-hafnia glasses and glass ceramics have been shown to be a good host for the erbium ions whose luminescence at about $1.5\,\mu m$ is widely employed in the telecommunications systems [140]. Recently [135], silica-hafnia glass-coated microspheres were produced and were found to exhibit similar luminescence properties like their planar waveguide counterparts as to the $1.5\,\mu m$ emission peak shape and position and to the luminescence decay lifetime. Starting from silica microspheres fabricated by melting a conventional telecommunication fiber, Er^{3+}-activated silica-hafnia layers were prepared by sol-gel route and dip-coating technique [134]. The starting solution, obtained by mixing TEOS, ethanol, deionised water and hydrochloric acid as a catalyst, was pre-hydrolysed for 1 hour at 65 °C. The molar ratio of TEOS : HCl : EtOH : H_2O was 1 : 0.01 : 37.9 : 2. An ethanolic colloidal suspension was prepared using as a precursor $HfOCl_2$ and then added to the TEOS solution, with a Si/Hf molar ratio of 70/30. Erbium was added as $Er(NO_3)_3 \times 5H_2O$ with a $Er/(Si + Hf)$ molar concentration ranging from 0.3 to 1 mol%. The final mixture was left at room temperature under stirring for 16 h. The obtained sol was filtered with a $0.2\,\mu m$ Millipore filter. Erbium-doped silica-hafnia layers were deposited on cleaned silica microsphere by dip-coating, with a dipping rate of 40 mm/min. Before further coating, each layer was annealed in air for 50 s at 900 °C. After a 10-dip cycle, the films were annealed for 2 min at 900 °C; the final coating, which could be the result of different numbers of dips (20 to 60), was stabilized by a last treatment for 5 min in air at 900 °C. Figure 25 shows the SEM image of the 1% mol Er^{3+}-activated $70SiO_2$-$30HfO_2$ film produced on top of the microsphere by 20 coating dips. No cracks are visible on the outer surface, but some defects appear, which could well be already present on the surface of the sphere before the deposition process; a roughness as low as about 1 nm was measured, suggesting that the global quality factor Q of the WGMR will not be limited by the surface quality of the coating.

Figure 26 compares the photoluminescence (PL) spectra relative to the $^4I_{13/2} \rightarrow {}^4I_{15/2}$ transitions of Er^{3+} ions for a coated microsphere (fig. 26(a)) and a planar waveguide (fig. 26(b)) based on the 0.3 mol% Er^{3+} activated $70SiO_2$-$30HfO_2$ system. The PL spectra in fig. 26 exhibit a main emission peak at $1.53\,\mu m$ with a shoulder at about $1.55\,\mu m$ and a bandwidth of 42 ± 1 nm. It is worth noting that no differences in shape and bandwidth are evident between the two PL spectra, indicating the full reproducibility of the sol-gel protocol.

Figure 27 shows the luminescence decay curves of the Er^{3+} $^4I_{13/2}$ metastable state obtained upon 980 nm excitation for microspheres coated by (a) 0.3, (b) 0.5, and (c) 1 mol% Er^{3+}-activated silica-hafnia films, respectively. The decay curves are single-exponential with lifetimes of 6.5, 4.7, and 3.3 ms, respectively. These values are compatible with the results obtained for $70SiO_2$-$30HfO_2$ planar waveguide doped with the same Er^{3+} content. In fact, as observed in the case of silica-hafnia planar waveguides, when the erbium concentration increases, the measured lifetime of the $70SiO_2$-$30HfO_2$ metastable state decreases. When increasing erbium content, the average distance between neighboring Er^{3+} ions decreases and the interaction between pairs of Er-Er ions becomes significant. The energy migration and upconversion processes can take place under this condition, lowering the fraction of excited Er^{3+} at a given pump power. Therefore, the decrease of the luminescence lifetime of the $^4I_{13/2}$ state as a function of the increasing Er^{3+} concentration occurs [141].
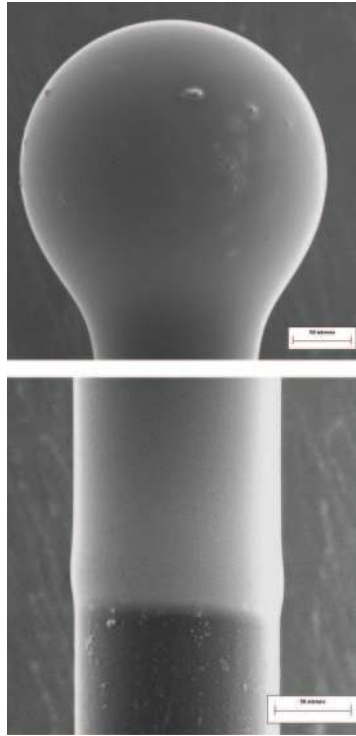
Fig. 25. – SEM image of 1% mol Er^{3+}-activated 70SiO$_2$-30HfO$_2$ films deposited on a silica microsphere using the sol-gel method (above) and the SEM image of the coated fiber on top of which the microsphere is located (below). The bar in the two photos is 50 μm [134].
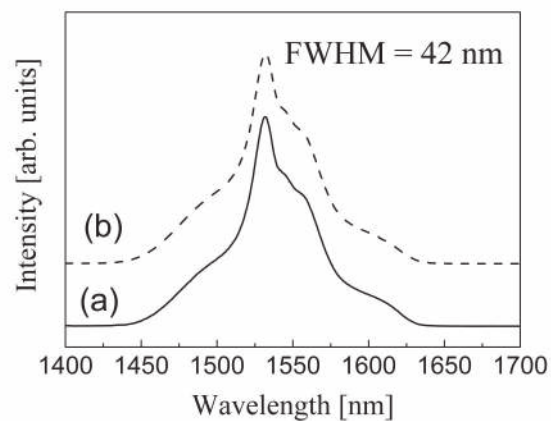

Fig. 26. – Photoluminescence spectra relative to the $^4I_{13/2} \rightarrow {}^4I_{15/2}$ transition of the Er^{3+} ions for (a) 0.3 mol% Er^{3+}-activated 70SiO$_2$-30HfO$_2$-coated silica microsphere and (b) planar waveguide obtained using the sol-gel method. Spectra were obtained upon excitation at 980 nm [134].
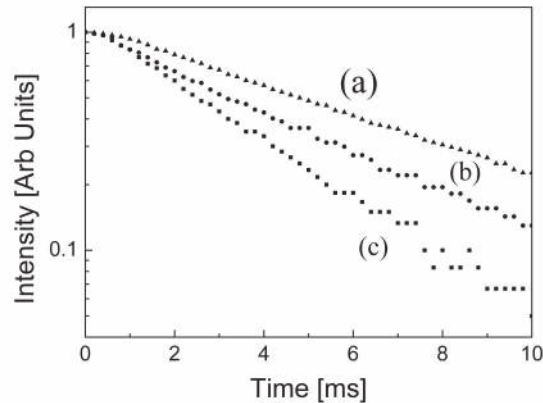
Fig. 27. – Decay curves of the $^4I_{13/2}$ metastable state of Er^{3+} ions in the 70SiO$_2$-30HfO$_2$-coated microspheres activated by (a) 0.3 mol% Er^{3+}, (b) 0.5 mol% Er^{3+}, and (c) 1 mol% Er^{3+} [134].

Figure 28 shows the 1.5 μm emission spectra of a 250 μm silica microsphere coated by a 70SiO$_2$-30HfO$_2$ film of 0.8 μm thickness, activated by 1 mol% Er^{3+}. Excitation of the WGMs was performed by a tapered fiber. The spectra were obtained for increasing values of the current of the pump laser at 1480 nm [133]. As the temperature of the spherical resonator is directly linked to the pump power at 1480 nm injected in the sphere, we would expect a shift in the resonance wavelengths. In the present case, however, the WGMR behavior seems to be quasi-independent on the pump power, at least in the range of interest, *i.e.* tens of mW. This important effect of the coating will be discussed further on in the next subsection.
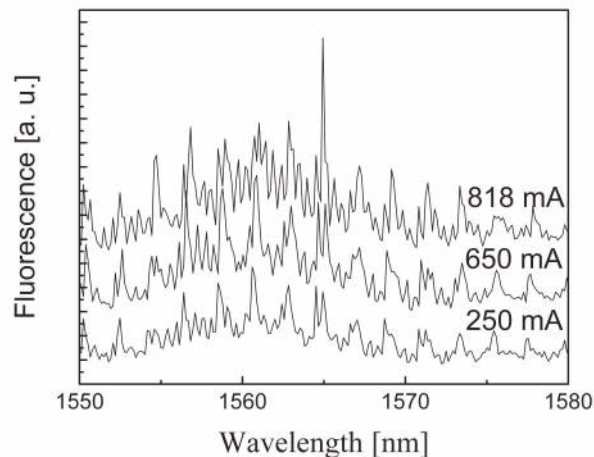

Fig. 28. – Fluorescence spectra measured for a 250 μm microsphere coated by a 70SiO$_2$-30HfO$_2$ film of 0.8 μm in thickness, activated by 1 mol% Er^{3+} for different values of the exciting pump power. In the figure the values of the exciting laser current are indicated [133].

We also coated a $430\,\mu$m silica microsphere by a 70SiO$_2$-30HfO$_2$ film of $1.1\,\mu$m thickness, activated by 0.1 mol% Er^{3+}. Looking at the luminescence spectrum, obtained upon 1480 nm excitation, where the two polarizations TE and TM for the mode $n = 1$ can be well resolved, from the spacing of the modes it was possible to calculate the refractive index $N = 1.56$ and the sphere diameter, which was confirmed to be $D = 430\,\mu$m $\pm\,10\,\mu$m, by using the formulas

$$(35) \qquad \Delta\lambda_{\ell,\ell+1} = \frac{\lambda^2}{\pi N D}\,, \qquad \Delta\lambda_{\mathrm{TE,TM}} = \Delta\lambda_{\ell,\ell+1}\frac{\sqrt{N^2-1}}{N}\,,$$

where D is the diameter of the microsphere. By looking closer at the emission spectra of this sphere we could also notice a degenerating effect of m. The maximal value of $|\ell - m|$, the azimutal index, can be estimated at 4. This degenerating effect finds its origin in the ellipticity of the sphere produced by the coating process. By measuring the spectral difference in wavelength between the two values of m, the ellipticity of the sphere can be deduced, and a value of 0.12% was found [133, 18].

5$\cdot$**2.** *Sol-gel glass-ceramic coatings*. – Glass-ceramics (GC) are nanocomposite materials which offer specific characteristics of capital importance in photonics. This kind of two-phase material is constituted by nanocrystals embedded in a glass matrix, and the respective volume fractions of crystalline and amorphous phase determine the properties of the glass-ceramic. Transparency is of particular importance when confined structures, such as dielectric optical waveguides and microresonators, are considered, and several works have been devoted to this topic [142, 143]. Silica-hafnia glass-ceramic coated microresonators were produced [136] with a procedure similar to that of the corresponding amorphous ones, the only difference being in the final heat treatment of the coated microspheres at 900 °C which lasted 20 minutes.

The PL spectrum of the GC-coated microsphere in fig. 29 (curve a) shows well-resolved Stark components typical of Er^{3+} emission in a crystalline-like environment. Moreover a
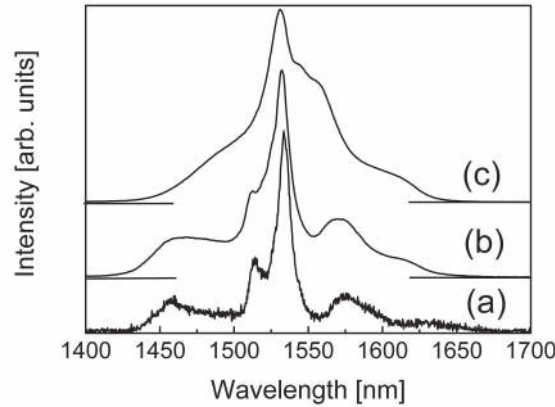

Fig. 29. – Room temperature photoluminescence spectra of the $^4I_{13/2} \rightarrow {}^4I_{15/2}$ transition of Er^{3+} ion for (a) spherical microresonator coated by a film of 70SiO$_2$-30HfO$_2$ activated by 0.3 mol% Er^{3+}, annealed for 20 min in air at 900 °C; (b) 70SiO$_2$-30HfO$_2$ glass-ceramic planar waveguide activated by 0.3 mol% Er^{3+}; (c) 70SiO$_2$-30HfO$_2$ amorphous planar waveguide activated by 0.3 mol% Er^{3+} [136].
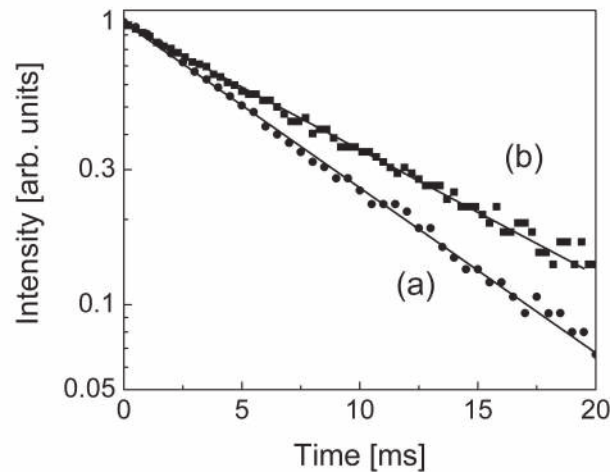
Fig. 30. – Decay curves of the luminescence from the $^4I_{13/2}$ metastable state of Er^{3+} ions for (a) $70SiO_2$-$30HfO_2$ glass-ceramic planar waveguide activated by $0.3\,mol\%$ Er^{3+}; (b) spherical microresonator coated by a glass-ceramic film of $70SiO_2$-$30HfO_2$ activated by $0.3\,mol\%$ Er^{3+} [136].

significant narrowing of the emission bandwidth is observed. These features are the fingerprint of a glass-ceramic system, as confirmed by the PL spectrum of the glass-ceramic waveguide (curve b). The bandwidth measured at $3\,dB$ from the maximum of the intensity was 51, 17, and $12\pm1\,nm$ for the amorphous waveguide (curve c), the GC waveguide, and the GC microresonator, respectively. The PL spectrum of the GC microresonator exhibits a more significant narrowing compared to that of the GC waveguide, indicating that in the case of microresonator there is a better homogeneity of the local environment where the Er^{3+} ion is accommodated. The decay curves of the metastable level $^4I_{13/2}$ are shown in fig. 30 for the glass-ceramic waveguide (fig. 30(a)) and the glass-ceramic microsphere (fig. 30(b)). Both the decays exhibit a single-exponential profile with a lifetime of 7.4 and $9.7\pm0.3\,ms$ for the waveguide and the microsphere, respectively. The observation of a single decay is a further indication of the high homogeneity of the rare earth local environment and in particular of the absence of a multi-site structure. A further evidence of the crystalline environment around erbium ions comes from the visible luminescence spectra, as shown in fig. 31. The important narrowing of the emission bands assigned to the $^4S_{3/2} \rightarrow {}^4I_{15/2}$ and $^2H_{11/2} \rightarrow {}^4I_{15/2}$ transitions of Er^{3+} ion and the well-evidenced Stark structures demonstrate that erbium ions are embedded in hafnia nanocrystals. Infrared and visible emission spectra, which do not exhibit any broadening typical of glasses, as well as single-exponential luminescence decays, are a strong indication that practically all the Er^{3+} ions are imbedded in HfO_2 nanocrystals.

5˙**3.** *Thermal effects of coatings*. – Another important application of transparent coatings onto spherical microresonators concerns the possibility of reducing the thermal shift of the WGM resonances due to microsphere heating by the dissipated pump energy. Actually, the shift is due both to the temperature-induced change in the refractive index (the thermo-optic coefficient) and to the temperature-induced increase of the diameter of the particle (coefficient of thermal expansion) [144]. Since the size parameter of the
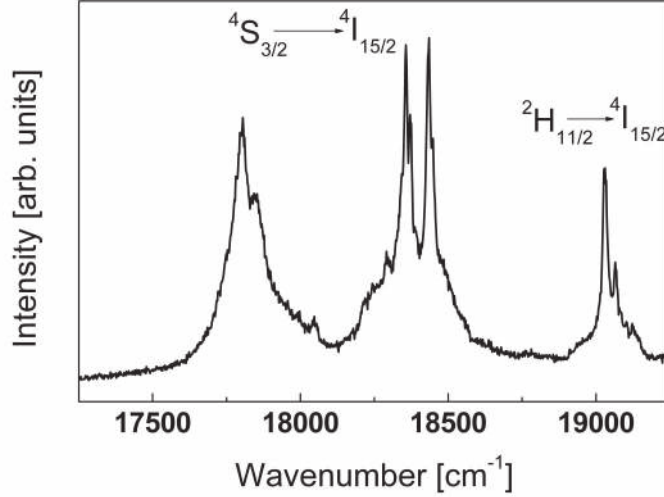
Fig. 31. – Room temperature luminescence spectra of the $^4S_{3/2} \rightarrow {}^4I_{15/2}$ and $^2H_{11/2} \rightarrow {}^4I_{15/2}$ transitions of Er^{3+} ion for a $100\,\mu$m microsphere coated with $70SiO_2$-$30HfO_2$ glass-ceramic layer [136].

WGM is equal to $x = 2\pi NR/\lambda$, where λ is the WGM wavelength, the increase of either the refractive index or the diameter of the microsphere must lead to the increase of the resonance wavelength for the size parameter to remain constant. Therefore

$$(36) \qquad \frac{1}{\lambda}\frac{\mathrm{d}\lambda}{\mathrm{d}T} = \alpha + \frac{1}{N}\frac{\mathrm{d}N}{\mathrm{d}T}\,,$$

where α is the thermal-expansion coefficient and N is the refractive index of the microsphere. One can also take advantage of this characteristic of the spherical WGMRs to accurately measure the thermo-optic coefficient of the material of which the microresonator is made [145]. For silica, which is the material most widely used for the production of microresonators, the thermo-optic coefficient $(\mathrm{d}N/\mathrm{d}T \approx 10^{-5})$ and the thermal expansion coefficient $(\alpha \approx 10^{-6})$ are both positive. Therefore, to compensate the thermal shift of the WGMs of the silica microsphere, a coating with a negative thermo-optical coefficient needs to be used. Again, there are two different mechanisms responsible for the temperature-induced change of the refractive index of a given material: the temperature-induced change of the absorption resonances of the material and the change of the density of the material (thermal expansion) [146]. If we suppose a simple oscillator model for the dispersion of the refractive index (Sellmeier equation)

$$(37) \qquad N^2 - 1 \propto \rho \frac{1}{E_0^2 - E^2}\,,$$

where ρ is the density of the material, then the thermo-optic coefficient is given by

$$(38) \qquad \frac{\mathrm{d}N}{\mathrm{d}T} = \frac{N^2-1}{2N}\left[-3\alpha - \frac{1}{E_0}\frac{\mathrm{d}E_0}{\mathrm{d}T}\frac{2E_0^2}{E_0^2 - E^2}\right],$$

where E is the photon energy and E_0 is the energy of the oscillator (for glasses E_0 corresponds to the energy of the band gap). Since for most glasses the position of the energy gap exhibits a red shift with the increase of temperature [147], the second part of eq. (38) will generally be positive in the transparent region of the glass absorption spectrum ($E \ll E_0$), becoming negative close to the band gap. Because of the low thermal expansion coefficient of most glasses, the second part of eq. (38) is usually dominant over the much smaller negative contribution of the thermal expansion contribution [147]: as a result, in most glasses the thermo-optic (TO) coefficient is positive, and therefore, according to eq. (36), the resonances of a glass microsphere will in general experience a red-shift upon the increase of temperature. On the other hand, the TO coefficient of most polymers is negative, because of the large value of their thermal expansion coefficient; measurements for a number of polymers have confirmed it and have shown that TO coefficients are directly proportional to their coefficients of thermal expansion [148].

Polymers can thus be considered good candidates for the stabilization of the WGMs; indeed, theoretical calculations have shown that polymer coatings as thin as 230 nm can fully compensate the thermal shift of the WGMs of a $100\,\mu$m silica microsphere [149]. Although there have been no attempts so far to experimentally confirm these theoretical calculations, a number of papers have recently been published on the thermal compensation of WGM resonances of microtoroids by both PDMS (polymethilsyloxane) [150] and by polymethylmethacrylate (PMMA) and polystyrene (PS) [151] coatings. The PS and PMMA coatings were demonstrated to be able to completely compensate the thermally induced shifts of the WGM resonances. As for the PDMS-coated microtoroids, since the refractive index of PDMS is lower than the refractive index of silica (unlike PS and PMMA, whose refractive indices are larger than silica), the compensation effect was found to strongly depend on the WGM resonance confinement inside the silica core of the microresonator. The more a given mode extends into the PDMS cladding, the more the compensation will be effective; it means that the compensation is much reduced for the fundamental WGM compared to higher-order modes.

Together with the efforts to use negative TO coefficient materials to stabilize the WGMs, efforts are also being made to coat the microspheres with highly positive TO coefficient materials, to be exploited for optical switching. In a material like silicon, with high thermo-optic coefficient ($\mathrm{d}N/\mathrm{d}T \approx 10^{-4}$) the temperature-induced shifts of the WGMs are large enough to ensure a complete transition from the resonant to the non-resonant condition at a given (signal) wavelenght. To test it, nanocrystalline silicon has been deposited on a silica microsphere [152]; depending on the 488 nm pump power, the 1450 nm WGM was demonstrated to shift from resonant to non-resonant condition. In the resonant condition, the incident 1450 nm signal is coupled to the microresonator resulting in zero transmission along the fiber (critical coupling). In the non-resonant condition the signal does not couple to the microsphere, resulting in almost complete transmission. Switching times of 25–30 ms have been measured with a very low switching peak power ($3.4\,\mu$W) [152].

In addition to the improvement of the thermal properties of WGMRs, the polymer coatings can also be usefully employed as a means of functionalizing the surface of a microresonator for immunosensing applications. In this case, the thickness and quality of the coating have to be optimized so as not to degrade the Q-factor of the microsphere. As an example, tests carried out with thin layers of different polymers have demonstrated that the microresonators still retain values of Q-factor high enough for use in sensing applications [52]. Further details at this regard are provided in the next section.

6. – Applications

In the previous sections we have already referred the reader to a number of possible applications of WGM resonators, such as narrow-band and add-drop optical filtering [153, 154, 35], feedback elements for external lasers [155-157], and multiwavelength and low-threshold lasers [144, 158, 159], just to mention a few examples.

An area, however, where WGMRs exhibit unique properties is that of sensing. The main advantage of a WGMR sensor is the fact that, if scattering losses by TIR at the boundary of the resonator are minimal and absorption of light in the material is very low, the trapped photons are able to circulate on their orbit several thousand times before exiting the WGMR by loss mechanism. This long lifetime of the confined photon is associated to a long optical path length because of the resonant nature of the phenomenon, namely to a very long interaction path. Detection of small forces, either mechanical or optical (optomechanics), is possible with very high sensitivity; the interested reader is referred to the review paper by Ward *et al.* [19].

Here we will focus on a specific area, that of biosensing by microspherical resonators, where very significant results have been achieved in the last years. When a micro- or nanoscopic object (of biological type too, like a bacterium or a molecule) is brought in contact with the confined circulating light, the interaction will be resonantly reinforced (reactive mechanism). The resulting change in radius and/or refractive index of the surface of the sphere induces, through the interaction with the evanescent part of the WGM field, a change in the Q-factor of the resonator or a shift in the resonance frequency: the sensitivity can be very high, such to detect single nanoparticles or single molecules.

6˙1. *Biosensors*. – The requirements for a biosensor are selectivity, sensitivity, stability and reversibility. These are mostly provided by the biochemical receptor (antibody, antigen, DNA, enzyme, aptamer), the sensitivity being also provided by the quality of the optical platform. Of the same importance are high signal-to-noise ratio (SNR), short response time, low limit of detection (LOD), integration capabilities and high sensitivity at low cost in real samples. For example, a common noise source in a WGM resonator is the temperature fluctuation, which results in undesirable thermo-optic and thermo-mechanic effects. Even though some authors claimed that the thermo-optic effect can greatly enhance the LOD, permitting to go down to single molecules, it has been proven that thermo-optic effects are far too small for enhancing the LOD [160]. A self-referenced WGM biosensor has been employed in order to reduce noise (thermal, non specific binding, etc.) [161].

Of critical importance for producing effective biosensors is the surface functionalization or chemical modification of the transducer's surface. Protein adheres to any glass surface increasing the unwanted non-specific effects. This crucial layer, however, has to be very thin, between 10 and 100 nm (below the evanescent penetration depth), and homogeneous in order to preserve the high quality of the transducer. There are several ways of functionalizing the surface of a biosensor, and the choice of the technique should take into account: high specificity, high affinity, stability and being detectable by an optical signal. The most common techniques are based on the silanization of the glass surface through covalent binding of the silane groups with the glass surface, and the use of biotin and/or streptavidin layers. The former shows a reduced non-specificity and enables a further functionalization with ligands or receptors [162-165], whereas the latter is based on a high-affinity binding with streptavidin and biotinylated molecules [166-168]. Very
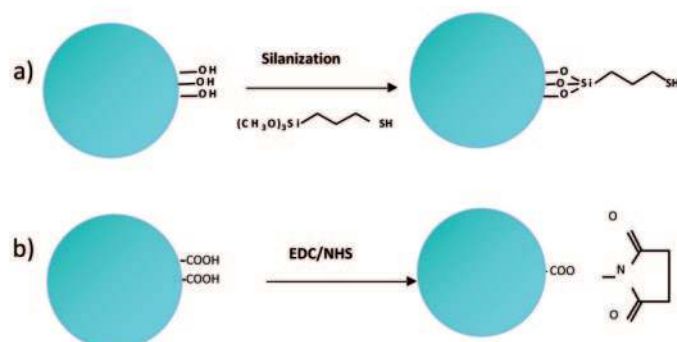
Fig. 32. – Scheme of the functionalization of a WGM sensor with: a) a silane agent; first, the microsphere surface has to be functionalized with primary amine groups, and later the receptors can be covalently bound to these groups. b) Eudragit; the carboxyl groups (COOH) are activated with EDC/NHS chemistry. Eudragit is a family of anionic copolymers based on methacrylic acid and methyl methacrylate.

recently, we demonstrated the feasibility of using polymer thin layers as functionalizing agents [52].

After silane and/or polymeric functionalization, the surface can be further modified for attachment to the recognition element of interest. This bioconjugation protocol is usually based on ester chemistry. 1-ethyl-3-[3-dimethylaminopropyl] carbodiimide hydrochloride (EDC) and N-hydroxysuccinimide (NHS) are commonly used to activate the functionalized surface [169, 52]. NHS reacts with primary amines on a recognition element to form a stable amide bond. Figure 32 shows an example of silanization process (fig. 32a) and the EDC/NHS bioconjugation protocol (fig. 32b).

Figure 33 shows a sketch of a biosensor based on WGM resonators, after the functionalization, interfaced with the biological recognition element. The middle row in fig. 33
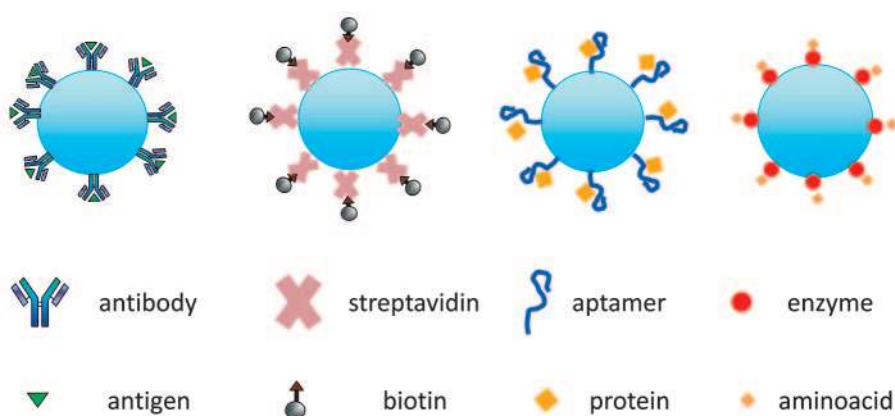

Fig. 33. – Top: schematic representation of a WGM biosensor, resulting from the combination of a WGMR with a sensing layer. Middle row: main ligands or receptors (antibodies, streptavidin, aptamers, enzymes). Bottom: main analytes (antigens, biotin(ylated) proteins, aminoacids).

shows a schematic representation of the most commonly used biological recognition elements: antibody, streptavidin, aptamer and enzyme; whereas the bottom row sketches the corresponding analytes: antigen, biotin/biotinylated proteins, proteins, and amino acids. Antibody-based sensors are called immunosensors while aptamer-based sensors are called aptasensors. The antibody shows high affinity and specificity towards the antigen, as conferred by their molecular complementarities. Enzymes are specific in both the reaction they catalyze and the substrate they recognize, and are subject to regulation of their activity by other molecules. Therefore, the use of enzymes can be advantageous owing to enzyme specificity and to the amplification phenomena given by enzyme catalysis. A major disadvantage is the dependence of the enzyme activity on physical and chemical environments. Aptamers are functional molecules exhibiting high specificity and affinity; even small changes in the target analyte may disrupt the binding. As they can in principle be selected *in vitro* for any given target, ranging from small molecules to large proteins and even cells, it is possible to develop a wide range of aptasensors.

Biosensors can also be classified on the basis of their assay format, either direct or indirect. A label-free biosensor is a direct assay [166] while an indirect assay is a labeled biosensor [167].

A quick analysis of the effect of an analyte on the WGM propagation can be performed by simply using geometrical optics. As we have already seen, at the sphere surface the condition to have resonance is that the optical path length, which is approximately equal to the circumference of the sphere, corresponds to an integer number of wavelengths:

$$(39) \qquad 2\pi a = \ell \frac{\lambda}{N} \, ,$$

with ℓ integer number, a the radius of the microsphere, N the refractive index and λ the wavelength of radiation. Therefore, the resonant wavelength changes can be written as

$$(40) \qquad \frac{\Delta\lambda}{\lambda} = \frac{\Delta a}{N} + \frac{\Delta N}{N} \, .$$

Such a heuristic approach is not valid when considering random coverage by complex molecules like proteins [170, 171]. Biomolecules binding to the WGMR surface shift the resonance due to their excess of polarizability, α_{ex} that is proportional to the molecular weight

$$(41) \qquad \frac{\Delta\lambda}{\lambda} = \frac{\alpha_{\mathrm{ex}}\sigma}{\epsilon_0(N_s^2 - N_m^2)a} \, ,$$

where σ is the surface density of molecules forming a layer, N_s and N_m are the refractive index of the sphere and the medium, respectively. Equation (41) describes only the shift but not the LOD. More detailed discussions about first-order perturbation theory for obtaining the shift can be found in [172, 173]. Assuming that the field of a particular biomolecule is not influenced by its neighbors [174] and taking into account that the lowest surface density that can be detected depends on the resonance linewidth $\delta\lambda$ (or a fraction F of the linewidth) which in turn depends on the quality factor Q [175], the LOD of surface density can be written as [169, 175]
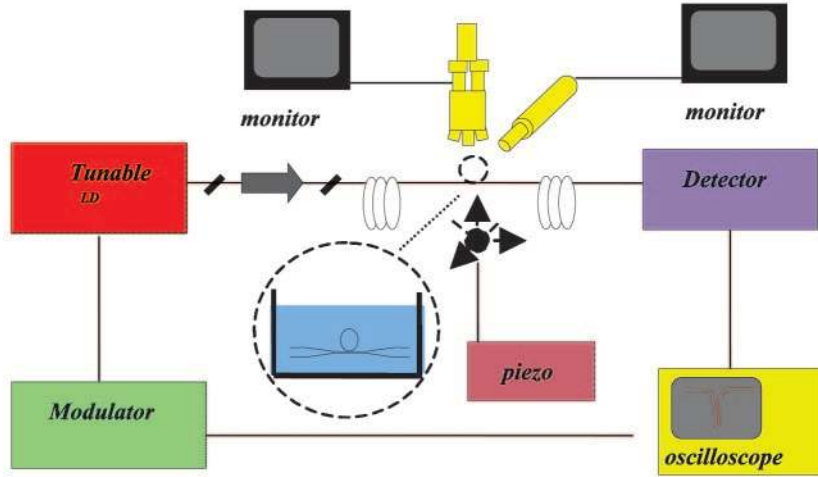
Fig. 34. – A schematic diagram of the experimental arrangement to follow resonance shifts of a microspherical WGMR in a liquid environment.

$$(42) \qquad \sigma_{\text{LOD}} = \frac{(\epsilon_0 a (N_s^2 - N_m^2) F)}{(\alpha_{\text{ex}} Q)} \,.$$

By using a narrow linewidth laser and scanning over a range of wavelengths, resonant wavelengths can be selectively excited and detected. Such laser can be finely swept at very low frequency around a resonance by a few GHz. The light transmitted through the coupler-WGM resonator system can be monitored at the output of the taper using a detector connected to an oscilloscope, as in the experimental set-up sketched in fig. 34.

Sample delivery is also a critical step in a biosensor device. Biochemical samples typically are in the form of aqueous solution; microfluidics is one of the most commonly used methods of sample delivery. Ideally, fluidics design should take into account sample injection and drainage, reduction of sample volume and detection time. Microsphere and taper integration are a quite challenging task; however, several attempts to integrate fluidics have been made. In early works [176, 163] small cuvettes and fluidic cells were used. The microsphere and the coupling taper were immersed in $1 \, \text{cm}^3$ of buffer solution, the fluidic system being temperature controlled and magnetically stirred for sample mixing (see fig. 35). Small fluidic cells have also been fabricated by using as a bottom window the coupling system itself, in that case constituted by either a fiber prism [177] or a bulky prism [168, 178].

A microfuidic flow system that incorporates the microsphere and the taper system is shown in fig. 36 [179, 169]. In this system, the taper is bound to a glass slide by an UV adhesive and acts as a foundation. This foundation is placed on top of a thermoelectric stage for temperature control. The microfluidic cell is made by replica moulding of a master in poly-dimethyl siloxane (PDMS). The cross-section of the microfluidic channel is $1.5 \, \text{mm} \times 2.5 \, \text{mm}$ and has a total volume of $100 \, \mu\text{L}$ [169]. Two computer-driven syringe pumps flow the sample and the buffer for washing between two sample injections, in order to avoid cross-sample contamination.
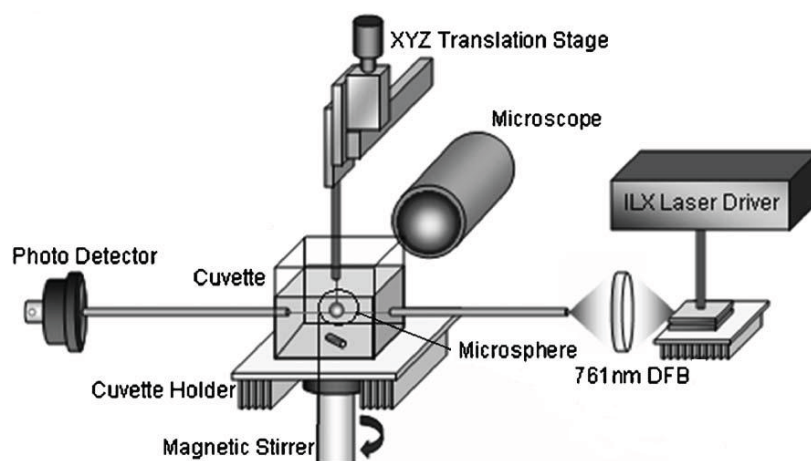
Fig. 35. – Experimental setup based on a disposable cuvette of $1\,cm^3$ volume, temperature controlled and magnetically stirred. (Reprinted with permission from [176] © 2005, American Institute of Physics.)
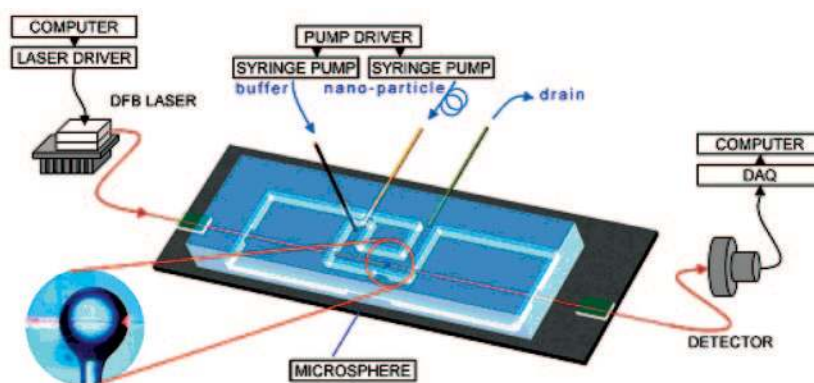

Fig. 36. – Microfluidic system for biosensing, incorporating a microsphere resonator and a coupling fiber. (Reprinted with permission from [179], © 2007, American Institute of Physics.)

6˙2. *Biomedical applications*. – The first experiment that demonstrated the quantitative use of WGM spherical microsensors in biomedicine dates back to 2002 [166]. In this early paper, specific detection of proteins was proven. A year later, the same group demonstrated the feasibility of multiplexed DNA quantification [162] and single nucleotide polymorphism analysis by hybridization. An unprecedented LOD of $6\,pg/mm^2$ was demonstrated. Specific and multiplexed DNA detection was performed by using two microspheres, allowing to discriminate a single nucleotide mismatch. Such technique could be of great use in detection of mutation of genes involved in cancer development without target labeling. In fig. 37 the time response of the two microspheres is shown. Sphere S1 was modified with a biotinylated 11-mer oligonucleotide (5′-biotin-CTATCTCAGTC), and the oligonucleotide immobilized on sphere S2 differed by a single
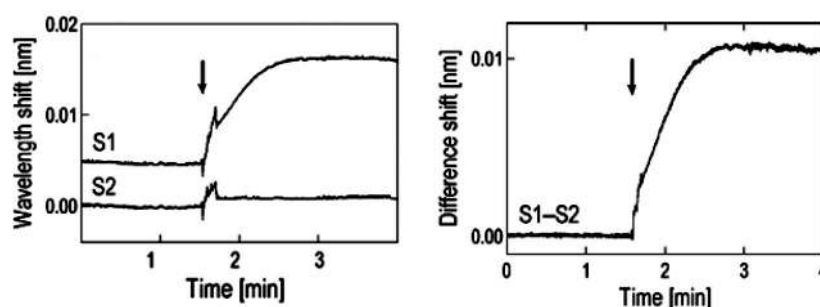
Fig. 37. – Single nucleotide mismatch detection. Left: time traces of the two microspheres, the shift for the perfect match sequence is 10 times larger; right: difference signal (SNR = 54). (Reprinted with permission from [162] © 2003, Elsevier.)

nucleotide (5′-biotin-CTATATCAGTC). The arrow indicates when the complementary oligonucleotide to the sequence of the one immobilized on S1 is injected (fig. 37, left). Spikes are due to transient temperature and refractive-index fluctuations, the difference of both signals allowing to indentify the mismatch with a signal-to-noise ratio (SNR) of 54 (fig. 37, right). The advantage of using two microspheres is obvious, as one can remove all common noise in experiments.

A similar scheme has been reported very recently [161]. The authors have theoretically demonstrated the capabilities of a biosensor consisting of two microspheres coupled to each other in a way that they behave as "photonic molecules" and can discriminate between bulk index changes and specific/non-specific surface binding events. The authors proposed as detection method the tracking of the bonding and antibonding optical modes.

An important clinical application for WGM biosensors is to detect proteolytic activity [163]. A number of neurotoxins, metabolic and cardiovascular markers participate in physiological processes through protein cleavage. In the work by Fan *et al.* [163], the BSA-trypsin pair is taken as a model system to model protein or peptide cleavage. BSA contains 60 lysine and 26 arginine residues that can be cleaved by trypsin. Partial removal of BSA molecules in the presence of trypsin results in a blue shift in the resonances. The LOD is equal to 10 pg/mL within 15 minutes.

An aptamer-based microspherical biosensor has been demonstrated for thrombin detection [164]. The minimum LOD experimentally tested was 5 NIH/mL (National Institute of Health units/mL) of thrombin, but a LOD of 1 NIH/mL could be estimated from the measurements performed. Control experiments to confirm the specific binding were carried out.

Identification of whole viruses has also been demonstrated [169]. The format used in this work is a direct immunosensor with the complementary antibody anchored to the surface of the microsphere. The model system here is a RNA virus known as MS2 that kills *E. coli* but is harmless to humans. The negative control is another *E. coli* virus, Phix174. Phix174 and MS2 are icosahedral viruses like HIV and their coat proteins contain different epitopes; Phix174, therefore, should not specifically bind to the surface-anchored anti-MS2. Figure 38 shows both sensorgrams. Phix174 was injected into the fluidic cell at 2.5 pM: the frequency shifted toward longer wavelengths and reached equilibrium before switching off the pump; 100 seconds later, PBS was injected into the cell and the wavelength dropped to the baseline, indicating the lack of covalent binding to the
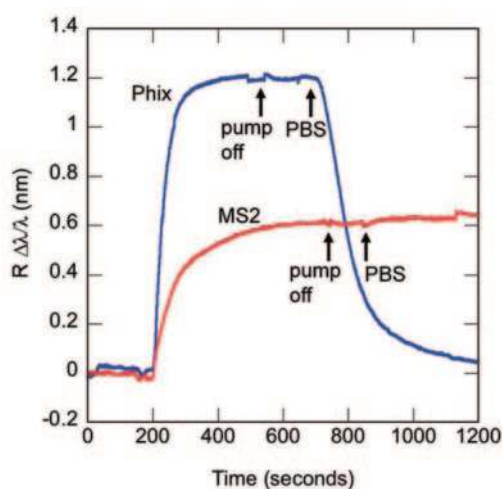
Fig. 38. – (Colour on-line) Comparison between Phix174 (blue line) and MS2 (red line) experiments on the same sphere. (Reproduced by permission of The Royal Society of Chemistry [169].)

anti-MS2. In the case of specific binding, after washing with PBS, there is no evidence of desorption. The arrows indicate the time when the pump is turned off and/or PBS was injected. The authors pushed further the LOD in the case of influenza A down to single virions, but in this latter experiment the sensing was non-specific [180].

WGMs can be excited with a polarized optical field. Such versatility can be very useful for measuring anisotropies in the biological layers covalently bond or adsorbed to the surface of the WGM resonator. Molecules attached themselves in preferred orientations: by comparing the measured shift ratio between the fields parallel and perpendicular to the surface with the theory, this preferred orientation can be determined [181]. The technique has been applied to study conformational changes in self-assembled monolayers such as biological membranes [182]. Even though the demonstration has been performed in a model system like bacteriorhodopsin, it has a very exciting future application: protein folding studies. Indeed, there are many diseases that result from misfolding of proteins or anomalous aggregations, like Parkinson's and Creutzfeldt-Jakob's disease, among many others. WGMRs can be combined with other optical techniques like, for instance, surface-enhanced Raman scattering (SERS) in order to measure the fingerprint of the bound molecules. It has been demonstrated theoretically that SERS can happen in WGM resonators without plasmons [183]. The feasibility has been proven for microspheres of high refraction index and small radii.

Microspherical resonators also provide a useful tool for studying larger biological material, such as micrometer-sized cells and bacteria. Analytic results were obtained for rod-like bacteria, relating the shift in wavelength and the broadening of the linewidth [184]. These results were confirmed by measuring *E. coli* (model system) with sensitivity of about 100 bacteria/mm^2. In this case the measurement was based on non-specific adsorption.

Active microspheres were proposed as sensor transducers with enhanced sensitivity [185]. The first demonstration was based on polymer microspheres doped with a gain medium, namely, a fluorescent dye like Rhodamine 6-G. The idea behind it was that

such microspheres could achieve narrower linewidths at lasing condition, and therefore increase the Q-factor by several orders of magnitude. The authors calculated that the LOD of active polystyrene microspheres could be 10^{-10} RIU (Refractive Index Units), beating Surface Plasmon Resonance sensors.

Specific detection of oligonucleotides was demonstrated by using silica microspheres functionalized with a fluorophore (tetra-methyl Rhodamine) and a dense monolayer of single strands of oligonucleotides [165]. The specific binding of the complementary strand caused shifts in the emission spectrum of the microsphere, being detected by an optical microscope and a CCD detector. The hybridization kinetics and the denaturation of the double-strand DNA was monitored at elevated temperatures; the hybridization was reversible. The authors obtained similar results with Q-dot-embedded microspheres: the WGMs were broader and less sensitive, but no photobleaching occurred.

Very recently, a new absolute WGM-based sensing method has been proposed, that does not require calibration, reference measurements or any prior knowledge about the microsphere radii [186]. Only one spectrum acquisition per fluorescent microsphere is needed. The authors proposed the use of free-floating functionalized fluorescent microspheres available commercially, reducing significantly the sample preparation. The proposed analytes are elongated spores of *Bacillus atrophaeus* subsp. *Golbigii* (*B. golbigii*). The authors used two different parameters for successful detection of the spores: the apparent refractive index and the calculated mean TE-TM mode spacing.

7. – Conclusions

In this review we have tried to summarize the main developments in the area of compact, mm- or μm-sized, whispering gallery mode resonators, characterized by extremely high-quality factors Q, up to 10^{11}. Their applications span from photonic engineering to quantum electrodynamics, to optical sensing and optomechanics. If spherical microdroplets and ring resonators have been among the first WGMRs, in the last few years microtoroids and microdisks have gained an increasing importance, also thanks to their good integrability; microspherical resonators, however, have continued to be widely investigated, due to their simple fabrication but also to their versatility. The choice of the material, in fact, allows one to produce either passive (*e.g.* narrow-band frequency filters) or active (*e.g.* microlasers) components; moreover, coating a microsphere with homogeneous, inhomogeneous, amorphous, or nanocomposite layers leads to the possibility of finely tuning the WGMR's thermodynamic, morphological, and optical properties.

Optimization of the coupling efficiency between the microcavity and a range of optical waveguides including fiber tapers and bulky prisms is still investigated, even if the use of the tapered fiber is considered to be one of the most efficient and flexible coupling means.

Several excellent results have been achieved in the last years, and the examples reported here represent only a very limited selection from the huge number of works performed in this field. In the telecommunications area, for instance, potential for all-fiber add-drop filters was demonstrated by using a bottle microresonator [35]. A number of rare-earth-doped and Raman microlasers with very low threshold have been demonstrated [187,105]. Also, due to the very high power density of the electromagnetic field of a WGM, and to the ongoing search for materials with higher and higher Kerr nonlinear coefficients and suitable for coating processes, very interesting perspectives exist for the development of nonlinear optical devices as key elements for the implementation of dense, ultra-fast all-optical signal processing [188,189].

Outstanding results have also been obtained in the field of optical sensing, and in particular in biosensing, where, for instance, single-virus detection from the frequency shift of a resonant WGM was demonstrated [180]. The success of the WGM approach arises from the combination of the exceptional sensitivity of the WGM resonances to refractive-index changes and from the long effective path length of the WGM within the resonator, which permits strong interaction between the circulating light and the adsorbed species. Finally, among the most recent advances, one can underline the integration of microresonators with microfluidics through the use of microcapillaries [38] and bubble microresonators [36, 37].

<p align="center">* * *</p>

REFERENCES

[1] Hall D. and Jackson P., *The Physics and Technology of Laser Resonators* (Taylor and Francis) 1989.
[2] Bykov V. and Silichev O., *Laser Resonators* (Cambridge Intl. Science Publ.) 1995.
[3] Kudryashov A. and Weber H., *Laser Resonators: Novel Design and Development* (SPIE Press) 1999.
[4] Hodgson N. and Weber H., *Laser Resonators and Beam Propagation*, 2nd edition (Springer) 2005.
[5] Dixit S. K., *Filtering Resonators* (Nova Science Publishers) 2001.
[6] Rabus D. G., *Integrated Ring Resonators: The Compendium* (Springer) 2007.
[7] Rayleigh L., *Philos. Mag.*, **20** (1910) 1001.
[8] Rayleigh L., *Scientific Papers*, **5** (1912) 617.
[9] Ashkin A. and Dziedzic J. M., *Appl. Opt.*, **20** (1981) 1803.
[10] Lam C. C., Leung P. T. and Young K., *J. Opt. Soc. Am. B*, **9** (1992) 1585.
[11] Wu J. H., Ang L. K., Liu A. Q., Teo H. G. and Lu C., *J. Opt. Soc. Am. B*, **22** (2005) 1770.
[12] Vahala K. J., *Nature*, **424** (2003) 839.
[13] Heebner J., Grover R. and Ibrahim T., *Optical Microresonators* (Springer) 2007.
[14] Matsko A., *Practical Applications of Microresonators in Optics and Photonics* (CRC Press) 2009.
[15] Richtmyer R. D., *J. Appl. Phys.*, **10** (1939) 391.
[16] Garret C., Kaiser W. and Bond W., *Phys. Rev. Lett.*, **15** (1961) 1807.
[17] Birks T. A., Knight J. C. and Dimmick T. E., *IEEE Phot. Techn. Lett.*, **12** (2000) 182.
[18] Chiasera A., Dumeige Y., Féron P., Ferrari M., Jestin Y., Nunzi Conti G., Pelli S., Soria S. and Righini G. C., *Laser Photon. Rev.*, **4** (2010) 457.

[19] WARD J. and BENSON O., *Laser & Photon. Rev.*, (2011) DOI: 10.1002/lpor.201000025.

[20] SUMETSKY M., *Opt. Express*, **18** (2010) 2413.

[21] SARMA J. and SHORE K. A., *IEE Proc. Optoelectron.*, **132** (1985) 325.

[22] MCCALL S. L., LEVI A. F. J., SLUSHER R. E., PEARTON S. J. and LOGAN R. A., *Appl. Phys. Lett.*, **60** (1992) 289.

[23] DJORDJEV K., CHOI S.-J., CHOI S.-J. and DAPKUS R., *IEEE Photon. Technol. Lett.*, **14** (Jun 2002) 828.

[24] BORSELLI M., SRINIVASAN K., BARCLAY P. E. and PAINTER O., *Appl. Phys. Lett.*, **85** (2004) 3693.

[25] ARMANI D. K., KIPPENBERG T. J., SPILLANE S. M. and VAHALA K. J., *Nature*, **421** (2003) 925.

[26] ARMANI D. K., MIN B. K., MARTIN A. L. and VAHALA K. J., *Appl. Phys. Lett.*, **85** (2004) 5439.

[27] KIPPENBERG T., SPILLANE S. and VAHALA K., *Phys. Rev. Lett.*, **93** (2004) 083904.

[28] HOSSEIN-ZADEH M. and VAHALA K. J., *Opt. Express*, **15** (2007) 166.

[29] RYU H. Y., KIM S. H., PARK H. G., HWANG J. K., LEE Y. H. and KIM J. S., *Appl. Phys. Lett.*, **80** (2002) 3883.

[30] SRINIVASAN K., BARCLAY P., PAINTER O., CHEN J., CHO C. and GMACHL C., *Appl. Phys. Lett.*, **83** (2003) 1915.

[31] LEE P., LU T., FAN J. and TSAI F., *Appl. Phys. Lett.*, **90** (2007) 151125.

[32] WHITE I. M., OVEYS H. and FAN X., *Opt. Lett.*, **31** (2006) 1319.

[33] ZAMORA V., DIEZ A., ANDRES M. V. and GIMENO B., *Photon. Nanostruct. Fundam. Appl.*, (2010) DOI:10.1016/j.photonics.2010.09.007.

[34] SUMETSKY M., *Opt. Lett.*, **29** (2004) 8.

[35] MURUGAN G. S., WILKINSON J. S. and ZERVAS M. N., *Opt. Lett.*, **35** (2010) 1893.

[36] SUMETSKY M., DULASHKO Y. and WINDELER R. S., *Opt. Lett.*, **35** (2010) 1866.

[37] SUMETSKY M., DULASHKO Y. and WINDELER R. S., *Opt. Lett.*, **35** (2010) 898.

[38] LI H., GUO Y., SUN Y., REDDY K. and FAN X., *Opt. Express*, **18** (2010) 25081.

[39] TZENG H., WALL K., LONG M. B. and CHANG R., *Opt. Lett.*, **9** (1984) 499.

[40] LIN H. B., EVERSOLE J. D. and CAMPILLO A. J., *Opt. Lett.*, **11** (1986) 614.

[41] DRUGER S., ARNOLD S. and FOLAN L. M., *J. Chem. Phys.*, **87** (1987) 2649.

[42] BISWAS A., LATIFI H., ARMSTRONG R. L. and PINNICK R. G., *Opt. Lett.*, **14** (1989) 214.

[43] SERPENGUZEL A., KUCUKSENEL S. and CHANG R. K., *Opt. Express*, **10** (2002) 1118.

[44] HARAGUCHI M., FUKUI M., TAMAKI Y. and OKAMOTO T., *J. Micros.*, **210** (2003) 229.

[45] SCHIRO P. G. and KWOK A. S., *Opt. Express*, **12** (2004) 2857.

[46] SHOPOVA S. I., FARCA G., ROSENBERGER A. T., WICKRAMANAYAKE W. M. S. and KOTOV N. A., *Appl. Phys. Lett.*, **85** (2004) 6101.

[47] SHIBATA S., ASHIDA S., SEGAWA H. and YANO T., *J. Sol-Gel Sci. Technol.*, **40** (2006) 379.

[48] WANG J., WANG M., LIU L., HAO W., HOU B. and LU Y., *J. Lumin.*, **122** (2007) 949.

[49] TERAOKA I. and ARNOLD S., *J. Opt. Soc. Am. B*, **24** (2007) 653.

[50] BELTAOS A. M. and MELDRUM A., *J. Lumin.*, **126** (2007) 607.

[51] DANTHAM V. R. and BISHT P. B., *J. Opt. Soc. Am. B*, **26** (2009) 290.

[52] SORIA S., BALDINI F., BERNESCHI S., COSI F., GIANNETTI A., NUNZI CONTI G., PELLI S. and RIGHINI G. C., *Opt. Express*, **17** (2009) 14694.

[53] DONG C.-H., SUN F.-W., ZOU C.-L., REN X.-F., GUO G.-C. and HAN Z.-F., *Appl. Phys. Lett.*, **2010** (96) 061106.

[54] LIN N., JIANG L., WANG S., YUAN L., XIAO H., LU Y. and TSAI H., *Appl. Opt.*, **49** (2010) 6463.

[55] LIN N., JIANG L., WANG S., XIAO H., LU Y. and TSAI H., *Appl. Opt.*, **50** (2011) 992.

[56] TREUSSART F., *Etude expérimentale de l'effet laser dans des microsphères de silice dopées avec des ions néodyme*, Ph.D. thesis, Université Pierre et Marie Curie (1997).

[57] GORODETSKY M., SAVCHENKOV A. and ILCHENKO V., *Opt. Lett.*, **21** (1996) 453.

[58] SAVCHENKOV A. A., MATSKO A. B., ILCHENKO V. S. and MALEKI L., *Opt. Express*, **15** (2007) 6768.

[59] DUMEIGE Y., TREBAOL S., GHIŞA L., NGUYÊN T. K. N., TAVERNIER H. and FÉRON P., *J. Opt. Soc. Am. B*, **25** (2008) 2073.

[60] VAN DE HULST H., *Optics of Spherical Particles* (Drukkerij J.F. Duwaer) 1946.

[61] BORN M. and WOLF E., *Principles of Optics* (Pergamon) 1980.

[62] KERKER, *The Scattering of Light, and other Electro-Magnetic Radiation* (Academic Press) 1969.

[63] STRATTON J., *Théorie de l'électromagnétisme* (Dunod) 1961.

[64] JACKSON J., *Classical Electrodynamics* (John Wiley and Sons) 1975.

[65] NUSSENZVEIG H., *Diffraction Effects in Semiclassical Scattering* (Cambridge University Press) 1992.

[66] ABRAMOWITZ M. and STEGUN I., *Handbook of Mathematical Functions* (Dover publications) 1970.

[67] SCHILLER S. and BYER R., *Opt. Lett.*, **16** (1991) 1138.

[68] TREBAOL S., *Etudes expérimentales des propriétés dispersives de structures photoniques à base de micro-résonateurs pour la réalisation de fonctions optiques*, Ph.D. thesis, Université de Rennes 1 (2010).

[69] GORODETSKY M. and FOMIN A., *IEEE J. Sel. Topics Quantum Electron.*, **12** (2006) 33.

[70] LISSILLOUR F., MESSAGER D., STÉPHAN G. and FÉRON P., *Opt. Lett.*, **26** (2001) 1051.

[71] FÉRON P., *Annales de la Fondation Louis de Broglie*, **29** (2004) 279.

[72] WEISS D., SANDOGHDAR V., HARE J., LEFEVRE-SEGUIN V., RAIMOND J.-M. and HAROCHE S., *Optics Lett.*, **20** (1995) 1835.

[73] VERNOOY D., ILCHENKO V., MABUCHI H., STREED E. and KIMBLE H., *Opt. Lett.*, **23** (1998) 247.

[74] BRAGINSKY V., GORODETSKY M. and ILCHENKO V., *Phys. Lett. A*, **137** (1989) 393.

[75] TIEN P., *Appl. Opt.*, **10** (1970) 2395.

[76] GORODETSKY M., PRYAMIKOV A. and ILCHENKO V., *J. Opt. Soc. Am. B*, **17** (2000) 1051.

[77] ORAEVSKY A., *Quantum. Electron.*, **32** (2002) 377.

[78] HAUS H., *Waves and Fields in Optoelectronics* (Prentice-Hall) 1984.

[79] TREBAOL S., NGUYÊN T. K. N., TAVERNIER H., GHIŞA L., DUMEIGE Y. and FÉRON P., *C. R. Phys. (Paris)*, **10** (2009) 964.

[80] CAI M., PAINTER O. and VAHALA K., *Phys. Rev. Lett.*, **85** (2000) 74.

[81] SLAGMOLEN B., GRAY M., BAIGENT K. and MCCLELLAND D., *Appl. Opt.*, **39** (2000) 3638.

[82] PANDIAN G. S. and SERAJI F. E., *Proc. IEE*, **138** (1991) 235.

[83] GORODETSKY M. L. and ILCHENKO V. S., *J. Opt. Soc. Am. B*, **16** (1999) 147.

[84] TREUSSART F., ILCHENKO V., ROCH J., HARE J., LEFÈVRE-SEGUIN V., RAIMOND J. M. and HAROCHE S., *Eur. Phys. J. D*, **1** (1998) 235.

[85] ILCHENKO V. S., YAO X. S. and MALEKI L., *Opt. Lett.*, **24** (1999) 723.

[86] KNIGHT J. C., CHEUNG G., JACQUES F. and BIRKS T. A., *Opt. Lett.*, **22** (1997) 1129.

[87] RAFIZADEH D., ZHANG J. P., HAGNESS S. C., TAFLOVE A., STAIR K. A., HO S. T. and TIBERIO R. C., *Opt. Lett.*, **22** (1997) 1244.

[88] PANITCHOB Y., MURUGAN G. S., ZERVAS M. N., HORAK P., BERNESCHI S., PELLI S., NUNZI CONTI G. and WILKINSON J. S., *Opt. Express*, **16** (2008) 11066.

[89] NUNZI CONTI G., BERNESCHI S., COSI F., PELLI S., SORIA S., RIGHINI G. C., DISPENZA M. and SECCHI A., *Opt. Express*, **19** (2011) 3651.

[90] IOANNIDIS Z., RADMORE P. and GILES I., *Opt. Lett.*, **13** (1988) 422.

[91] POIRSON J., BRETENAKER F., VALLET M. and FLOCH A. L., *J. Opt. Soc. Am. B*, **14** (1997) 2811.

[92] MAZZEI A., GÖTZINGER S., DE S. MENEZES L., ZUMOFEN G., BENSON O. and SANDOGHDAR V., *Phys. Rev. Lett.*, **99** (2007) 173603.

[93] TREBAOL S., DUMEIGE Y. and FÉRON P., *Phys. Rev. A*, **81** (2010) 043828.

[94] SAVCHENKOV A. A., MATSKO A. B., ILCHENKO V. S. and MALEKI L., *Opt. Express*, **15** (2007) 6768.

[95] GRUDININ I. S., MATSKO A. B. and MALEKI L., *Opt. Express*, **15** (2007) 3390.

[96] REICK F. G., *Appl. Opt.*, **4** (1965) 1396.

[97] SUMETSKY M. and DULASHKO Y., *OSA Proc. OFC-2006*, (2006) paper O1T4u0L76.

[98] POON A. W., CHANG R. K. and LOCK J. A., *Opt. Lett.*, **23** (1998) 1105.

[99] NAM S. and YIN S., *IEEE Photon. Technol. Lett.*, **17** (2005) 2391.

[100] YANG R., YUN A., ZHANG Y. and PU K., *Optik*, **122** (2011) 900.

[101] SUMETSKY M., DULASHKO Y. and GHALMI S., *Opt. Lasers Eng.*, **48** (2010) 272.

[102] RÖSS D., *Proc. IEEE*, **51** (1963) 468.

[103] WALSH P. and KEMENY G., *J. Appl. Phys.*, **34** (1963) 956.

[104] GRUDININ I. S. and MALEKI L., *Opt. Lett.*, **32** (2007) 166.

[105] GRUDININ I. and MALEKI L., *J. Opt. Soc. Am. B*, **25** (2008) 594.

[106] NUNZI CONTI G., BERNESCHI S., COSI F., PELLI S., SORIA S., RIGHINI G. C., DISPENZA M. and A. S., *Opt. Express*, **19** (2011) 3651.

[107] KIPPENBERG T., SPILLANE S., ARMANI D. and K. J. V., *Opt. Lett.*, **29** (2004) 1224.

[108] JAGER J. B., NOE P., PICARD E., CALVO V., DELAMADELEINE E. and HADJI E., *Physica E*, **41** (2009) 1127.

[109] TRAN V.-T., BENOÎT J.-P. and VENIER-JULIENNE M.-C., *Int. J. Pharmaceut.*, **407** (2011) 1.

[110] KAWAGUCHI K., *Prog. Polym. Sci.*, **25** (2000) 1171.

[111] IOPPOLO T., KOZHEVNIKOV M., STEPANIUK V., ÖTÜGEN M. and SHEVEREV V., *Appl. Opt.*, **47** (2008) 3009.

[112] DONG C.-H., HE L., XIAO Y.-F., GADDAM V., OZDEMIR S., GUO H.-C. and YANG L., *Appl. Phys. Lett.*, **94** (2009) 231119.

[113] LI H., LEI L., ZENG Q., SHI J., LUO C., JI H., OUYANG Q. and CHEN Y., *Sensors Actuators B*, **145** (2010) 570.

[114] PENG X., SONG F., JIANG S., PEYGHAMBARIAN N., KUWATA-GONOKAMI M. and XU L., *Appl. Phys. Lett.*, **82** (2003) 1497.

[115] MIURA K., TANAKA K. and HIRAO K., *J. Non Cryst. Solids*, **213-214** (1997) 276.

[116] KITAMURA N., MAKIHARA M., HAMAI M., SATO T., MOGI I., AWAJI S., WATANABE K. and MOTOKAWA M., *Jpn. J. Appl. Phys.*, **39** (2000) L324.

[117] KITAMURA N., MAKIHARA M., SATO T., HAMAI M., MOGI I., AWAJI S., WATANABE K. and MOTOKAWA M., *J. Non-Cryst. Solids*, **293-295** (2001) 624.

[118] NUNZI CONTI G., CHIASERA A., GHISA L., BERNESCHI S., BRENCI M., DUMEIGE Y., PELLI S., SEBASTIANI S., FÉRON P., FERRARI M. and RIGHINI G. C., *J. Non-Cryst. Solids*, **352** (2006) 2360.

[119] BICA I., *Mater. Sci. Engin. B*, **77** (2000) 210.

[120] VOLLMER F., *Resonant detection of nano to microscopic objects using whispering gallery modes*, PhD Thesis, The Rockefeller University (2004).

[121] BRENCI M., CALZOLAI R., COSI F., NUNZI CONTI G., PELLI S. and RIGHINI G. C., *Proc. SPIE*, **6158** (2006) 61580S.

[122] COLLOT L., LEFÈVRE-SEGUIN V., BRUNE B., RAIMOND J. and HAROCHE S., *Europhys. Lett.*, **23** (1992) 327.

[123] STOBER W., FINK A. and BOHN E., *J. Colloid. Interface Sci.*, **26** (1968) 62.

[124] DE DOOD M. J. A., BERKHOUT B., VAN KATS C. M., POLMAN A. and VAN BLAADEREN A., *Chem. Mater.*, **14** (2002) 2849.

[125] RIGHINI G. C., ARMELLINI C., CHIASERA A., JESTIN Y., FERRARI M., CHIAPPINI A., MONTAGNA M., DUVERGER C. A., FÉRON P., BERNESCHI S., BRENCI M., NUNZI CONTI G., PELLI S., GONÇALVES C. and ALMEIDA R., *Glass Technol.: Eur. J. Glass Sci. Technol. A*, **48** (2007) 200.

[126] KARMAKAR B., DE G. and GANGULI D., *J. Non-Cryst. Solids*, **272** (2000) 119.

[127] HOI P. V., HA C. T. T. and HUNG H. Q., *Appl. Phys. Lett.*, **87** (2005) 161110.

[128] VON KLITZING W., LONG R., ILCHENKO V. S., HARE J. and LEFEVRE-SEGUIN V., *Opt. Lett.*, **26** (2001) 166.

[129] Louyer Y., Meschede D. and Rauschenbeutel A., *Phys. Rev. A*, **72** (2005) 031801.

[130] Pöllinger M. O. D. W. F. and Rauschenbeutel A., *Phys. Rev. Lett.*, **103** (2009) 053901.

[131] Murugan G., Wilkinson J. and Zervas M., *Opt. Express*, **17** (2009) 11916.

[132] Aden A. L. and Kerker M., *J. Appl. Phys.*, **22** (1951) 1242.

[133] Righini G. C., Berneschi S., Nunzi Conti G., Pelli S., Moser E., Retoux R., Féron P., Gonçalves R., Speranza G., Jestin Y., Ferrari M., Chiasera A., Chiappini A. and Armellini C., *J. Non-Cryst. Solids*, **355** (2009) 1853.

[134] Ngoc C. T., Huy P. T., Chien N. D., Ferrari M., Chiasera A., Armellini C., Moser E., Montagna M., Chiappini A., Brenci M., Nunzi Conti G., Pelli S. and Righini. G. C., in *Proceedings of the International Conference on Engineering Physics, Hanoi, Oct. 9-12, 2006* (Hanoi University Press) 2006.

[135] Righini G. C., Cosi F., Nunzi Conti G., Pelli S., Soria S., Moser E., Jestin Y., Ferrari M., Féron P., Chiasera A., Chiappini A. and Armellini C., *Phys. Status Solidi A*, **206** (2009) 898.

[136] Alombert-Goget G., Armellini C., Berneschi S., Chiasera A., Cosi F., Nunzi Conti G., Féron P., Ferrari M., Lunelli L., Moser E., Pederzolli C. and Righini G. C., *IEEE Proc. ICTON Mediterranean Winter Conference, 2009*, doi:10.1109/ICTONMW.2009.5385639.

[137] Pavesi L., Negro L. D., Mazzoleni C., Franz G. and Priolo F., *Nature*, **408** (2000) 4410.

[138] Ristić D., Holý V., Ivanda M., Marciuš M., Buljan M., Gamulin O., Furiić K., Ristiić M., Musiić S., Mazzola M., Chiasera A., Ferrari M. and Righini G. C., *J. Mol. Struct.*, **993** (2011) 214.

[139] Yang L. and Vahala K., *Opt. Lett.*, **28** (2003) 592.

[140] Gonçalves R. R., Carturan G., Zampedri L., Ferrari M., Montagna M., Righini G. C., Pelli S., Ribeiro S. J. L. and Messaddeq Y., *Opt. Mater.*, **25** (2004) 131.

[141] Ferrari M., *Active sol-gel materials, fluorescence spectra and lifetimes* in *Handbook of Sol Gel Science and Technology*, edited by Sakka S., Vol. **II**, *Characterization of sol-gel materials and products* (Kluwer - Academic Publishers) 2005.

[142] Tick P., *Opt. Lett.*, **23** (1998) 1904.

[143] Mattarelli M., Montagna M. and Verrocchio P., *Appl. Phys. Lett.*, **91** (2007) 061911.

[144] Cai Z., Chardon A., Xu H., Féron P. and Stéphan G., *Opt. Commun.*, **203** (2002) 301.

[145] Hryciw Z., Kekatpure R. D., Yerci S., Negro L. D. and Brongersma L. M., *Appl. Phys. Lett.*, **98** (2011) 041102.

[146] Wemple S. H., *Phys. Rev. B*, **7** (1971) 3767.

[147] Ghosh G., *Appl. Opt.*, **36** (1997) 1540.

[148] Zhang Z., Zhao P., Lin P. and Sun F., *Polym. Commun.*, **47** (2006) 4892.

[149] Han M. and Wang A., *Opt. Lett.*, **32** (2007) 1800.

[150] He L., Xiao F., C. C. D., Zhu J., V. V. G. and Yang L., *Appl. Phys. Lett.*, **93** (2008) 201102.

[151] Choi H. S. and Armani A. M., *Appl. Phys. Lett.*, **97** (2010) 223306.

[152] Tewary A., Digonnet M. J. F., Sung J. Y., Shin J. H. and Brongersma M. L., *IEEE J. Sel. Topics Quantum Electron.*, **12** (2006) 1476.

[153] Bilici T., Isci S., Kurt A. and Serpenguzel A., *IEEE Photon. Technol. Lett.*, **16** (2004) 476.

[154] Gilardi G., Donisi D., Serpenguzel A. and Beccherelli R., *Opt. Lett.*, **34** (2009) 3253.

[155] Vassiliev V., Velichansky V., Ilchenko V., Gorodetsky M., Hollberg L. and Yarovitsky A., *Opt. Commun.*, **158** (1998) 305.

[156] Lissillour F., Gabet R., Féron P., Besnard P. and Stéphan G., *Europhys. Lett.*, **55** (2001) 499.

[157] Sprenger B., Schwefel H. G. L. and Wang L. J., *Opt. Lett.*, **34** (2009) 3370.

[158] YANG L., ARMANI D. K. and VAHALA K. J., *Appl. Phys. Lett.*, **83** (2003) 825.

[159] HOI P. V., HA C. T. T. and HUNG H. Q., *Appl. Phys. Lett.*, **87** (2005) 161110.

[160] ARNOLD S., SHOPOVA S. and HOLLER S., *Opt. Express*, **18** (2010) 281.

[161] BORISKINA S. and DAL NEGRO L., *Opt. Lett.*, **35** (2005) 2496.

[162] VOLLMER F., ARNOLD S., BRAUN D. T. I. and LIBCHABER A., *Biophys. J.*, **85** (2003) 1974.

[163] HANUMEGOWDA N. M., WHITE I. M., OVEYS H. and FAN X., *Sensor Lett.*, **3** (2005) 315.

[164] ZHU H., SUTER J. D., WHITE I. M. and FAN X., *Sensors*, **6** (2006) 785.

[165] NUHIJI E. and MULVANELY P., *Small*, **3** (2007) 1408.

[166] VOLLMER F., BRAUN D., LIBCHABER A., KHOSHSIMA M., TERAOKA I. and ARNOLD S., *Appl. Phys. Lett.*, **80** (2002) 4057.

[167] NADEAU J. L., ILCHENKO V. S., KOSSAKOVSKI D., BEARMAN G. H. and MALEKI L., *Proc. SPIE*, **4629** (2002) 172.

[168] LIN Y., ILCHENKO V., NADEAU J. and MALEKI L., *Proc. SPIE*, **6452** (2007) 64520U.

[169] ARNOLD S., RAMJIT R., KENG D., KOLCHENKO V. and TERAOKA I., *Faraday Discuss.*, **137** (2008) 65.

[170] ARNOLD S., KHOSHSIMA M., TERAOKA I., HOLLER S. and VOLLMER F., *Opt. Lett.*, **28** (2003) 272.

[171] TERAOKA I. and ARNOLD S., *J. Appl. Phys.*, **102** (2007) 076109.

[172] TERAOKA I., ARNOLD S. and VOLLMER F., *J. Opt. Soc. Am. B*, **20** (2003) 1937.

[173] TERAOKA I. and ARNOLD S., *J. Opt. Soc. Am. B*, **23** (2006) 1381.

[174] TERAOKA I. and ARNOLD S., *J. Appl. Phys.*, **101** (2007) 023505.

[175] VOLLMER F. and ARNOLD S., *Nature Methods*, **5** (2008) 591.

[176] NOTO M., KOSHSIMA M., KENG D., TERAOKA I., KOLCHENKO V. and ARNOLD S., *Appl. Phys. Lett.*, **87** (2005) 223901.

[177] HANUMEGOWDA N. M., STICA C. J., PATEL B. C., WHITE I. M. and FAN X., *Appl. Phys. Lett.*, **87** (2005) 201107.

[178] WESTCOTT S., ZHANG J., SHELTON R., BRUCE N., GUPTA S., KEEN S., TILLMAN J., WALD L., STRECKER B., ROSENBERGER A., DAVIDSON R., CHEN W., DONOVAN K. and HRYNIEWICZ J., *Rev. Sci. Instrum.*, **79** (2008) 033106.

[179] KENG D., MCANANAMA S. R., TERAOKA I. and ARNOLD S., *Appl. Phys. Lett.*, **91** (2007) 103902.

[180] VOLLMER F., ARNOLD S. and KENG D., *Proc. Natl. Acad. Sci. U.S.A.*, **105** (2008) 20701.

[181] NOTO M., KENG D., TERAOKA I. and ARNOLD S., *Biophys. J.*, **92** (2007) 4466.

[182] TOPOLANCIK J. and VOLLMER F., *Biophys. J.*, **92** (2007) 2223.

[183] AUSMAN L. and SCHATZ G., *J. Chem. Phys.*, **129** (2008) 054704.

[184] REN H.-C., VOLLMER F., ARNOLD S. and LIBCHABER A., *Opt. Express*, **15** (2007) 17410.

[185] YANG J. and GUO L., *IEEE J. Sel. Topics Quantum Electron.*, **12** (2006) 143.

[186] CHARLEBOIS M., PAQUET A., VERRET L. S., BOISSINOT K., BOISSINOT M., BERGERON M. G. and ALLEN C. N., *Nanoscale Res. Lett.*, **5** (2010) 524.

[187] MENG L., ROOS P. and CARLSTEN J., *J. Quantum. Electron.*, **40** (2004) 390.

[188] PÖLLINGER M. and RAUSCHENBEUTEL A., *Opt. Express*, **18** (2010) 17764.

[189] RAZDOLSKIY I., BERNESCHI S., NUNZI CONTI G., PELLI S., MURZINA T. V., RIGHINI G. C. and SORIA S., *Opt. Express*, **19** (2011) 9523.